Topic	Examples of interactive data analysis of seismic records using the SEISAN software
Authors	**Lars Ottemöller**, Department of Earth Science, University of Bergen, Bergen, Norway, lars.ottemoller@geo.uib.no **Peter Bormann** (formerly GFZ German Research Centre for Geosciences, Dept. 2, D-14473 Potsdam, Germany); E-mail: pb65@gmx.net
Version	April 2013; **DOI: 10.2312/GFZ.NMSOP-2_IS_11.7**

Note: Figure numbers followed in this text by ?? relate to the NMSOP editions 2002 (printed) and 2009 (website). They will be changed when the revised Chapter 11 of NMSOP-2 becomes available.

page

1 Introduction

The purpose of this information sheet is to illustrate the steps involved when analyzing seismic records by means of the SEISAN software. Examples are given for local, regional and teleseismic earthquakes. This is done by giving representative screen plots together with explanatory texts that follow the figures.

For details on the SEISAN software the reader is referred to section 11.4.2 (Data Analysis and Seismogram Interpretation - Software for routine analysis – SEISAN) and the references therein. Details of the software commands are not given here, and the reader is referred to the SEISAN manual for details, which can be downloaded either from NMSOP-2 via the link 'Download programs and files' or from
ftp://ftp.geo.uib.no/pub/seismo/SOFTWARE/SEISAN/ .

The events are included with the sample data that is available with SEISAN (from version 9.2).

The main background material provided by NMSOP-2 (http://nmsop.gfz-potsdam.de), explaining the methodology behind this information sheet, is:

- CHAPTER 2: Seismic Wave Propagation and Earth Models
- CHAPTER 3: Seismic Sources and Source Parameters
- CHAPTER 5: Seismic Sensors and their Calibration
- CHAPTER 6: Seismic Recording Systems
- CHAPTER 11: Data Analysis and Seismogram Interpretation
- IS 2.1: Standard nomenclature of seismic phases
- IS 3.3: The new IASPEI standards for determining magnitudes from digital data and their relation to classical magnitudes
- IS 11.1: Seismic source location
- IS 11.4: Tutorial for consistent phase picking at local to regional distances
- DS 2.1-2.4: Record examples for local, regional and teleseismic earthquakes and explosions

Note that there are in the following some, only apparent, differences between SEISAN internal nomenclature and procedures and those recommended by the IASPEI standards for measuring magnitudes which do not contradict. While SEISAN mb and IASPEI mb are identical, SEISAN mB corresponds to IASPEI mB_BB. Similarly holds that SEISAN Ms = Ms_20 and MS = Ms_BB. Moreover, IASPEI standards recommend to measure mB_BB and Ms_BB on unfiltered broadband velocity traces, however accompanied by the statement that their passband should cover at least the period range within which these two magnitudes should be measured. SEISAN, however, always deconvolves any given actual record so as to simulate for mB_BB a velocity-proportional broadband response in the period range between 0.2 and 30 s and for Ms_BB a response in the period range between 3 and 60 s. This allows in SEISAN to read the broadband magnitudes also on short-period records, provided that the SNR is sufficient to allow a broadband velocity restitution.

2 Analysis of a local earthquake in southern Norway recorded between 50 km and 650 km epicentral distance

The earthquake chosen here as example occurred in southern Norway and was recorded on the Norwegian National Seismic Network operated by the University of Bergen. The event was recorded on a mix of short-period and broadband seismic stations. It was automatically detected and then interactively processed.

The earthquake parameters are:

Date:	14 Mar 2012
Origin time:	19:22:27.9 (UTC)
Latitude:	59.526°N
Longitude:	5.615°E
Depth:	13.9 km
ML:	3.4

We now show the step-by-step procedure to analyze the earthquake.

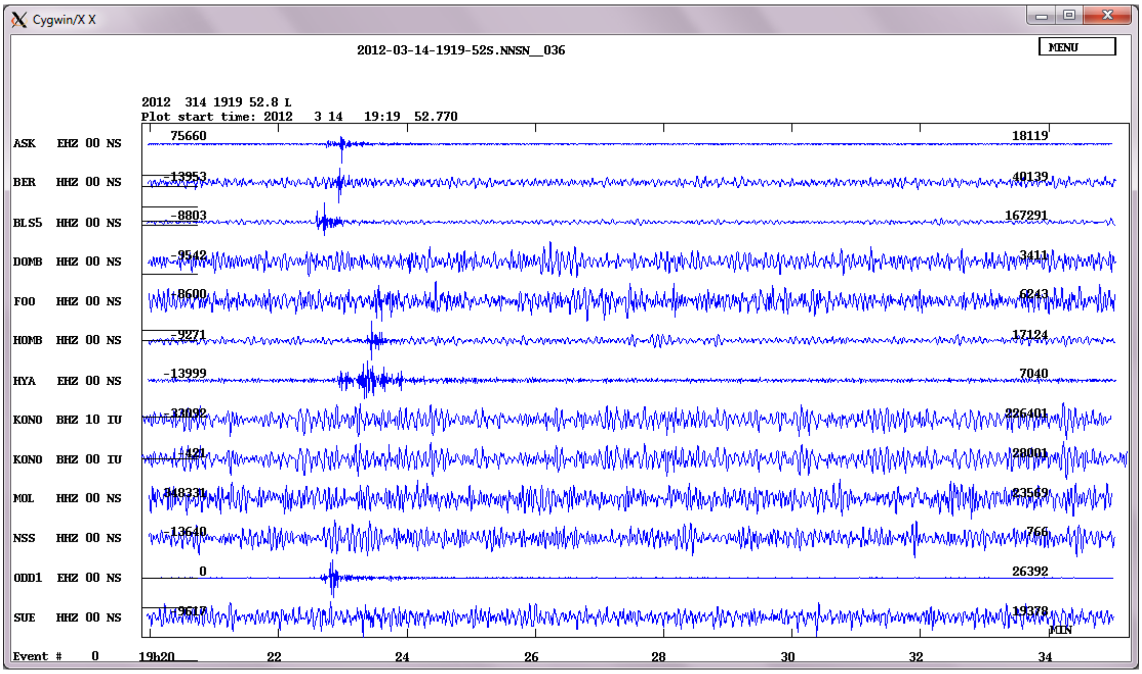

Vertical-component traces, unfiltered: Our starting point is a waveform file that is produced by an automatic detection system. No additional information is given, although, depending on the automated processing system, additional information including type of event, location and magnitude may already be available. It is our first task to identify the type of event that is recorded. If the detection is not false, the initial choices are between local, regional and teleseismic event. It may also be possible to identify if the event is likely an explosion based on the characteristics of the waveforms and the pattern of phase arrival times. The above multi-trace plot shows records of a small local earthquake, characterized by the short signal duration of less than about 1 min and a relatively high frequency signal content.

The event is recorded on 13 seismic stations. The numbers on the SEISAN multi-trace plot gives the DC of individual traces on the left and the maximum zero to peak amplitude on the right. The units are counts unless instrument correction is used to compute displacement, velocity or acceleration with the units nm (nanometers = 10^{-9} m), nm/s and nm/s^2, respectively. Station and component codes are given left of each trace together with the location code and network code. For the first trace, the station is ASK, the component is EHZ (short-period seismometer, with high sampling rate of more than 80 samples per second), the location code is 00 (used to indicate differences between equipment that gives the same component code at the same site, for example an STS2 at 40sps is labeled BHZ.00 and an STS1 at 20sps is labeled BHZ.10) and the network is NS (indicating who operates the station, in this case NS = Norwegian National Seismic Network). The event is well visible on the short-period seismometer records, which have the component code EHZ. However, it is not seen on the broadband traces, which are labeled HHZ, as this is a small earthquake where the signal content is mostly above 0.5 Hz.

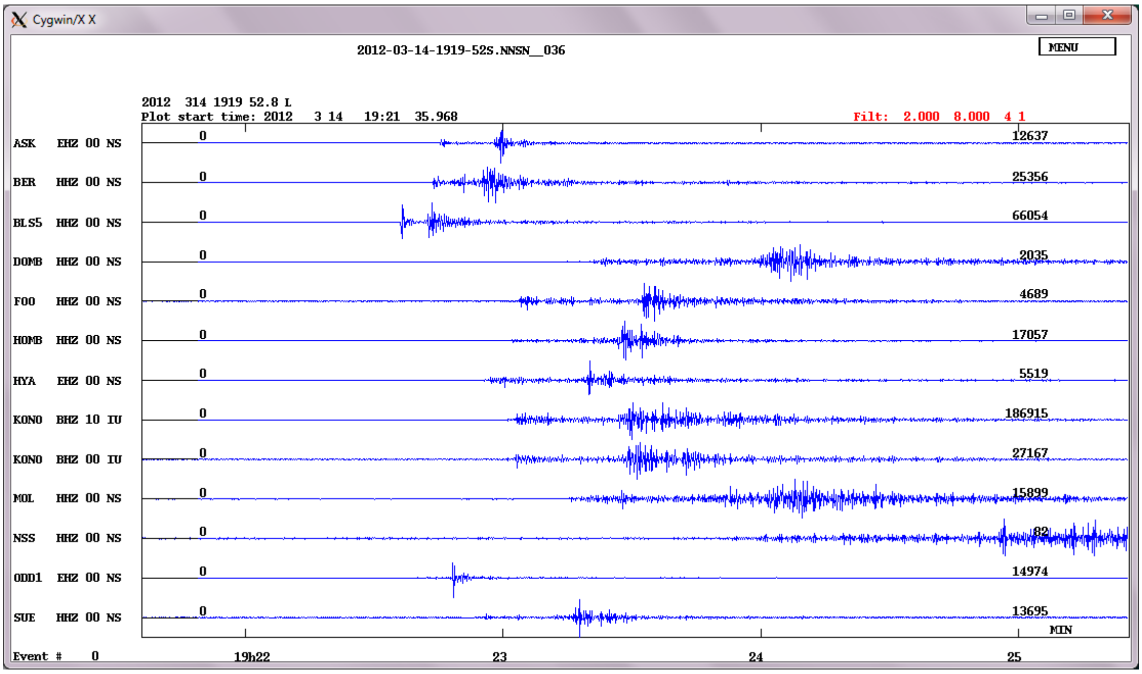

Vertical-component traces, filtered 2-8 Hz: Applying this high-frequency band-pass filter, which suppresses the more long-period microseismic noise in the broadband records, the earthquake is now clearly seen on all the traces. As compared to the previous plot, the time window of signal arrivals has been cut out and the time scale been stretched. With distinct primary P- and secondary S-wave arrivals in this frequency band it is very clear that this is a local earthquake. We can see from the arrival times that the earthquake was closest to station BLS5. In SEISAN we then put this event into the database and start the processing.

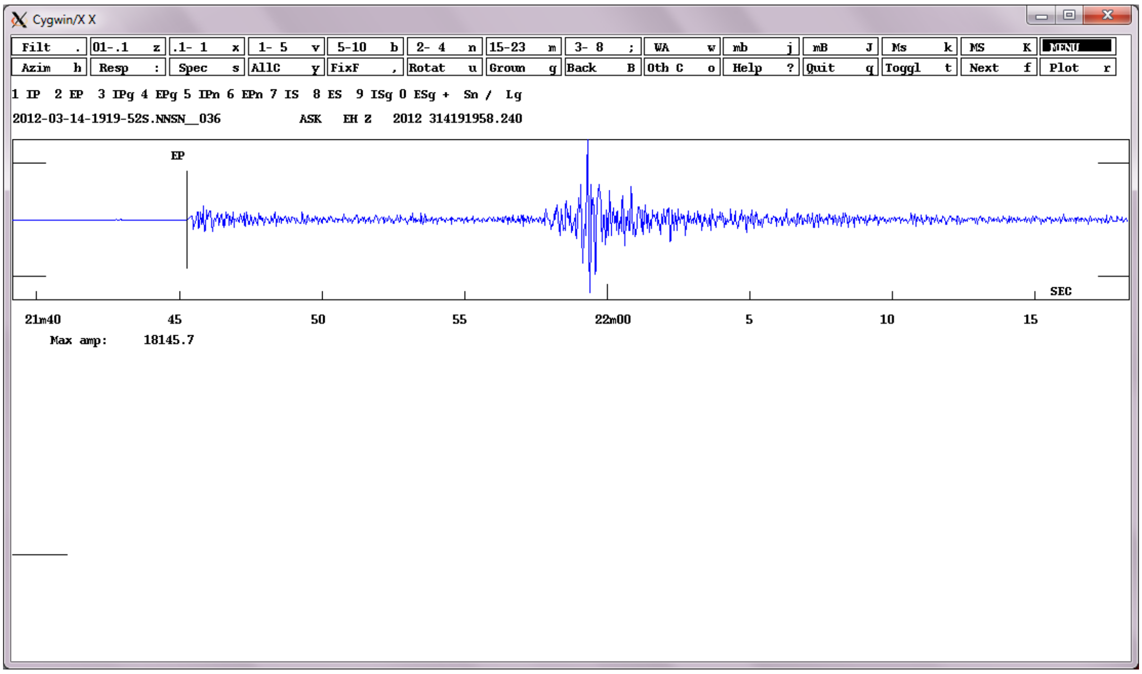

Single trace plot of station ASK at epicentral distance of 109 km, unfiltered: In SEISAN, we mostly do the phase picks on single trace plots, like shown here, or on three-component trace plots. For this recording on a short-period seismometer it is not necessary to filter the data in order to pick phase arrivals. The P arrival is marked.

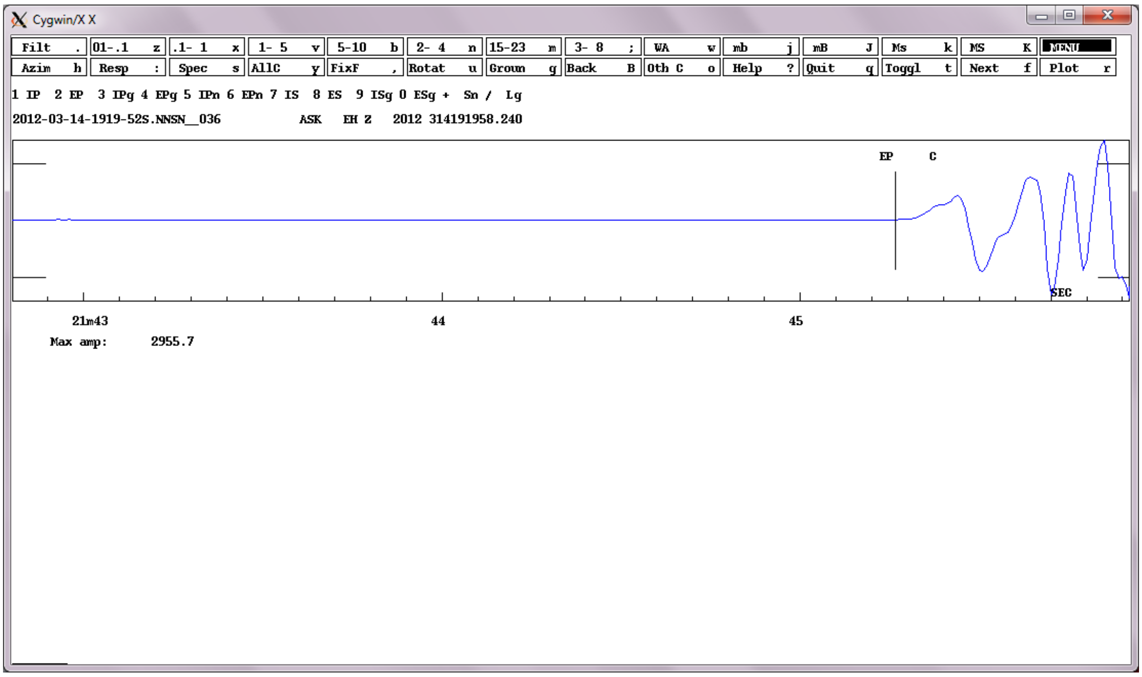

Single-trace plot of station ASK at epicentral distance of 109 km, unfiltered: This is the same station as on the previous plot, but this time we have zoomed in on the P arrival. It is now possible to read the P arrival time more accurately, and we can also identify the polarity of the first arrival, which is compression (upward motion on the vertical component) in this case. The phase arrivals will be used for the earthquake location (see IS 11.1) and the polarity can be used to determine the fault plane solution (see also EX 3.2).

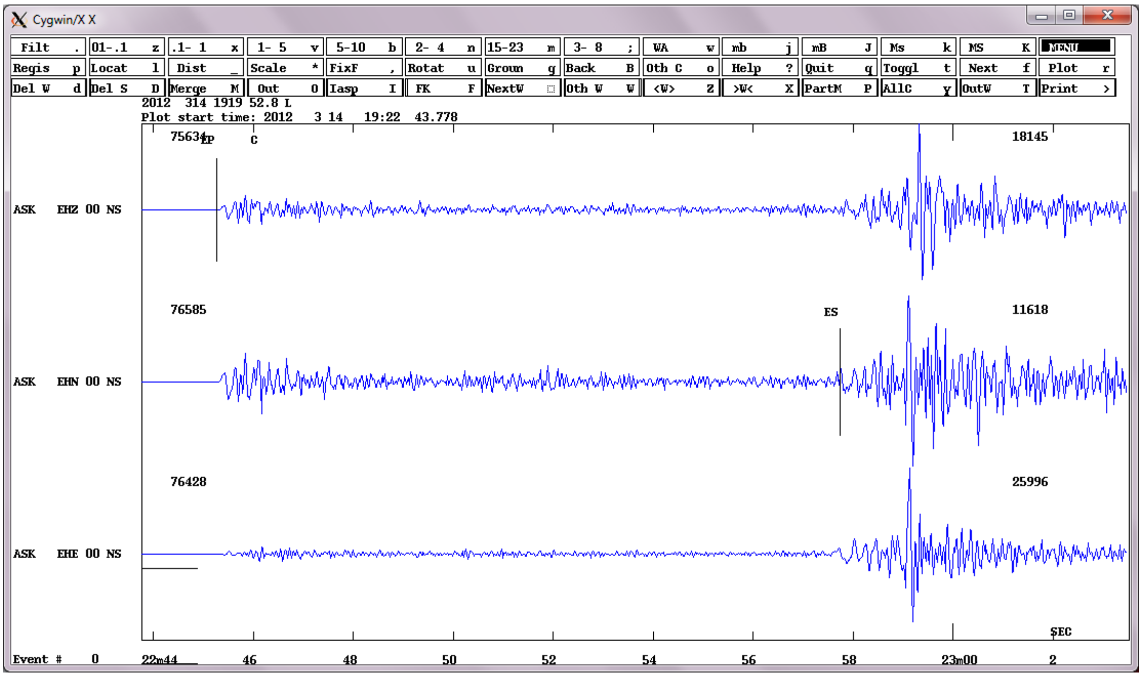

Three-component trace plot of station ASK at epicentral distance of 109 km, unfiltered: We normally read the S arrival on one of the two horizontal channels and not on the vertical as SP conversions may arrive prior to S and result in an incorrect reading of the onset time.

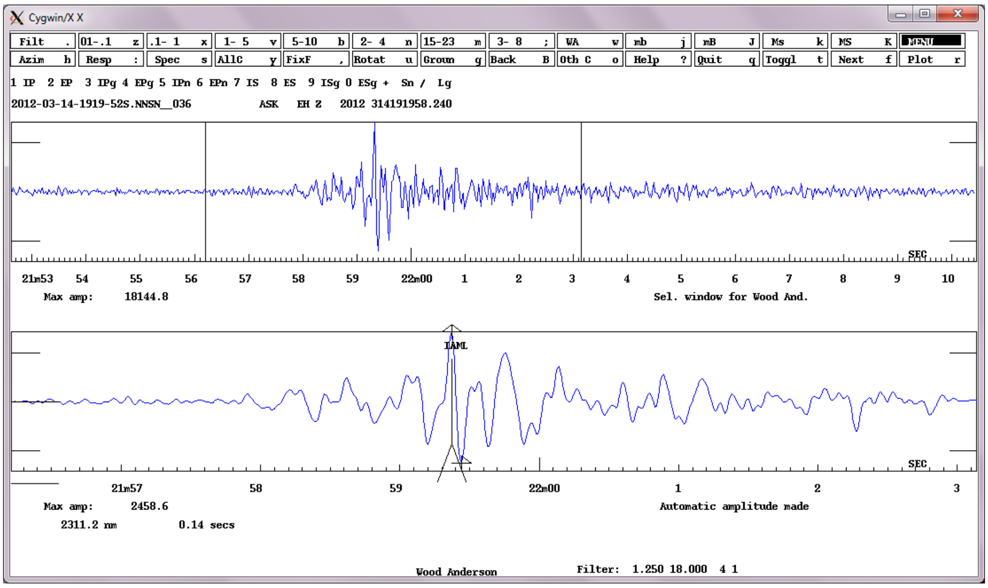

Single-trace plots of station ASK at epicentral distance of 109 km, Wood-Anderson filter: To read the ML amplitude, the instrument response is removed and a filter equivalent to the revised Wood-Anderson seismograph response according to Uhrhammer and Collins (1990) (see also IS 3.3) is applied. The bottom trace is a zoomed-in version of the area between the two vertical lines on the top trace. In SEISAN the amplitude is given in units of nanometer. It is measured peak-to-adjacent trough of the maximum deflection of the seismogram trace, where peak and trough are separated by one crossing of the zero-line (sometimes described as "peak-to-peak amplitude") but stored in the database is peak-to-peak/2 according to the IASPEI (2013) standard. This maximum amplitude is normally read from the S or Lg waves. It is stored as the IAML amplitude phase. 'I' stands for IASPEI standard, assuring that the standard Wood-Anderson filter response and the recommended amplitude measurement procedure has been applied (see IS 3.3), and '**A**' stands for displacement amplitude in nm. IASPEI standard for ML is to measure A on horizontal components. In Norway, however, it is routine practice to use the vertical component for the amplitude reading of ML and the scale given by Alsaker et al. (1991; see also DS 3.1, Tab. 2). This scale was derived for Norway and scaled so that its results match at 60 km distance with those of the horizontal component California standard formula for equal IAML input (see next figure and recommendations in IS 3.3). The default ML formula implemented in SEISAN is that of Hutton and Boore (1987; see next figure and formula in DS 3.1, Tab. 2), on which also the IASPEI standard formula for ML is based (see IS 3.3). If, however, this default procedure is used in other regions with other attenuation conditions then the calculated Ml values may differ from standard ML. DS 3.1. Table 2, offers several Ml calibration functions for other regions together with comments on their scaling, components to be used and the distance range of their applicability. You may implement in SEISAN either your own properly to the ML standard scaled local calibration function, or, if not yet available, one of those which you believe to match best with the seismotectonic conditions in the area. Note, however, that local Ml data based on not yet tested and proven standard scaling should not be published with the nomenclature for standard ML. That is, why we use in NMSOP Ml as the general nomenclature for local magnitude, and ML only for Ml that has been properly scaled to the new standard. Otherwise, users of local magnitude data do not know whether or not they have been correctly scaled according to the now globally set standard. E.g., according to Braunmiller et al. (2005) (see also section 3.2.9.6 in the forthcoming new Chapter 3) the Ml scales used by various agencies in Southern Germany, France, Italy and Switzerland yield results for equal input data that differ on average between 0.2 to 0.6 m.u. when scaled to Mw.

Some examples for other regional Ml calibration functions have been plotted in the diagram below. Note that the Alsaker et al. (1991) scale (lowermost full line) for the continental shield areas of Scandinavia and Eurasia reveals significantly lower attenuation when compared with Southern California calibration curves of both Richter (1935) and Hutton and Boore (1987) (see full dot and open dot curves in the Figure below). Accordingly, since properly scaled to the latter at about 60 km epicentral distance, the Alsaker et al. calibration curve yields at several 100 km distance for equal amplitude input data already ML values that are several tenths of magnitude units smaller than those derived by applying the original Richter scale. This difference increases to 1.7 m.u. at a distance of 1500 km, up to which the Alsaker et al. (1991) scale is defined (although strictly Hutton and Boore (1987) is limited to 600 km).

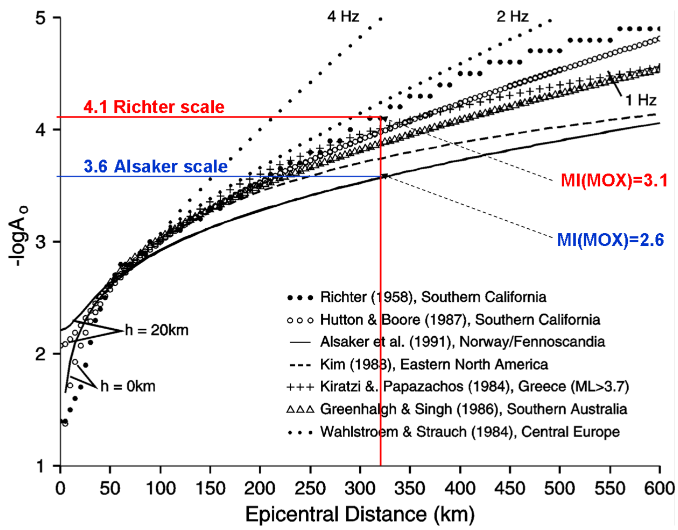

We now repeat the same procedure of measuring IAML for the other stations, however show only examples from some selected stations to explain specific aspects of the data processing.

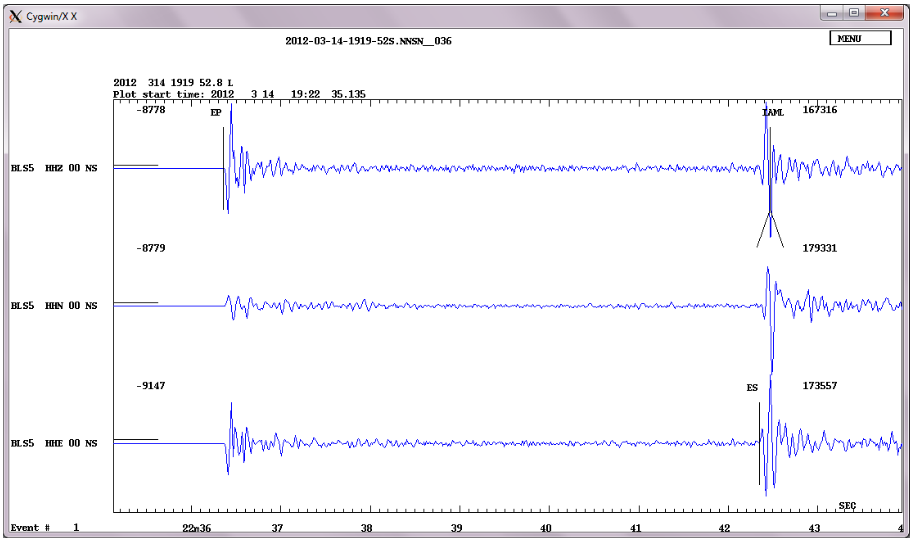

Three-component traces of station BLS5 at epicentral distance of 49 km, unfiltered: Plotted are the three-component broadband traces from the nearest station. P and S arrivals, and the ML amplitude were read. In this case the SNR was high enough so that it was not necessary to filter the broadband recordings to identify the phase arrivals.

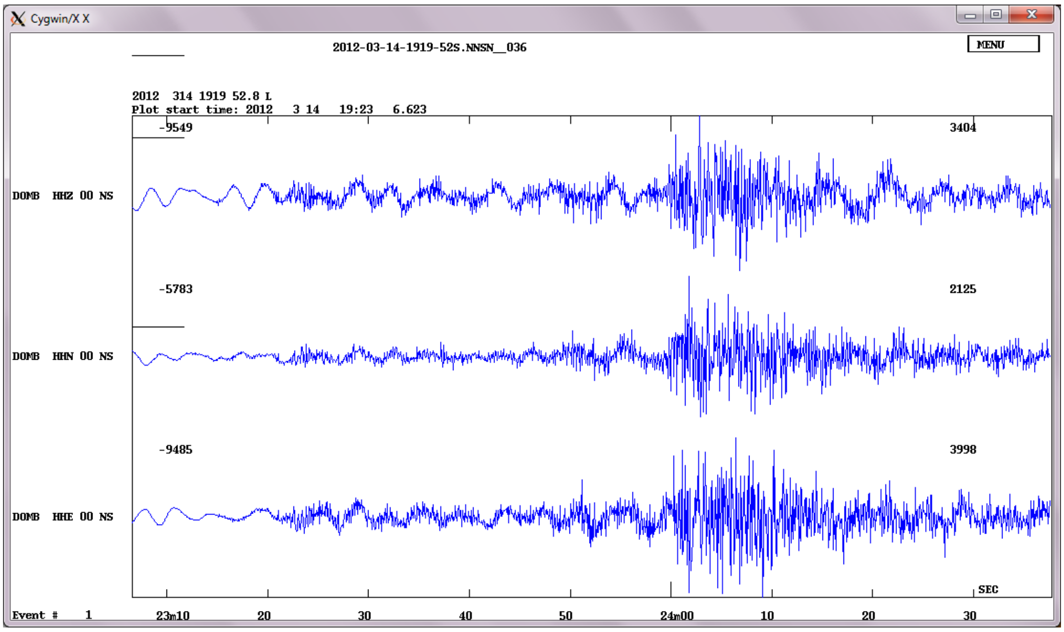

Three-component traces of station DOMB at epicentral distance of 342 km, unfiltered: Going to larger distances, the signal amplitudes at higher frequencies decrease relative to the more low-frequency microseismic noise, which peaks around 5 seconds. Here, we would normally filter the traces to read the phase arrivals.

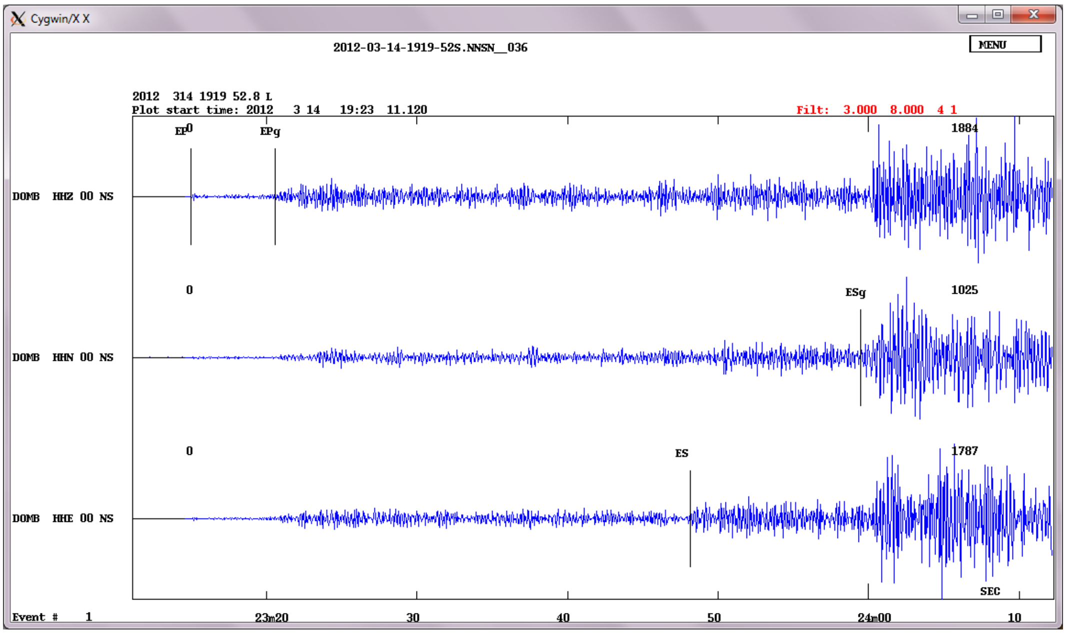

Three-component traces of station DOMB at epicentral distance of 342 km, filtered 3-8 Hz: For this station, it is possible to read besides the larger amplitude P and S arrivals, termed Pg and Sg, additionally the commonly weaker but earlier arrivals Pn and Sn. In SEISAN we generally mark the first P- and S-wave arrivals as P and S, respectively. The location program then determines which phase arrives first. Sometimes, Sn (here marked as ES) is weak and not recognizable in the signal-generated noise of scattered P waves. Then one has to mark Sg as such, since the location program otherwise would use it as the first arriving S (Sn in this case).

Reading different phases with different take-off angle from the source, such as Pg/Pn and Sg/Sn, significantly improves the depth determination. However, one should be quite certain that these identifications are correct. This requires fairly clear arrivals, an experienced analyst and that the phases match the solution when locating. For standard nomenclature, nature and travel paths of crustal phases see IS 2.1 and for many more record examples DS 11.1.

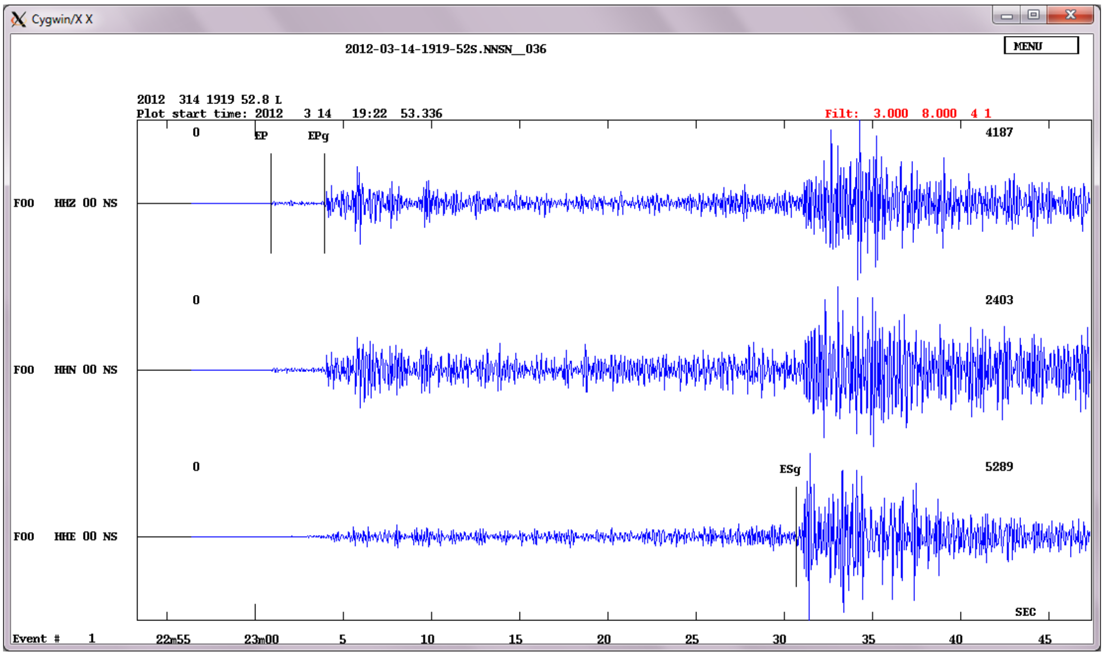

Three-component traces of station FOO at epicentral distance of 233 km, filtered 3-8 Hz: This is an example where Sn cannot be read, and S has to be read as Sg.

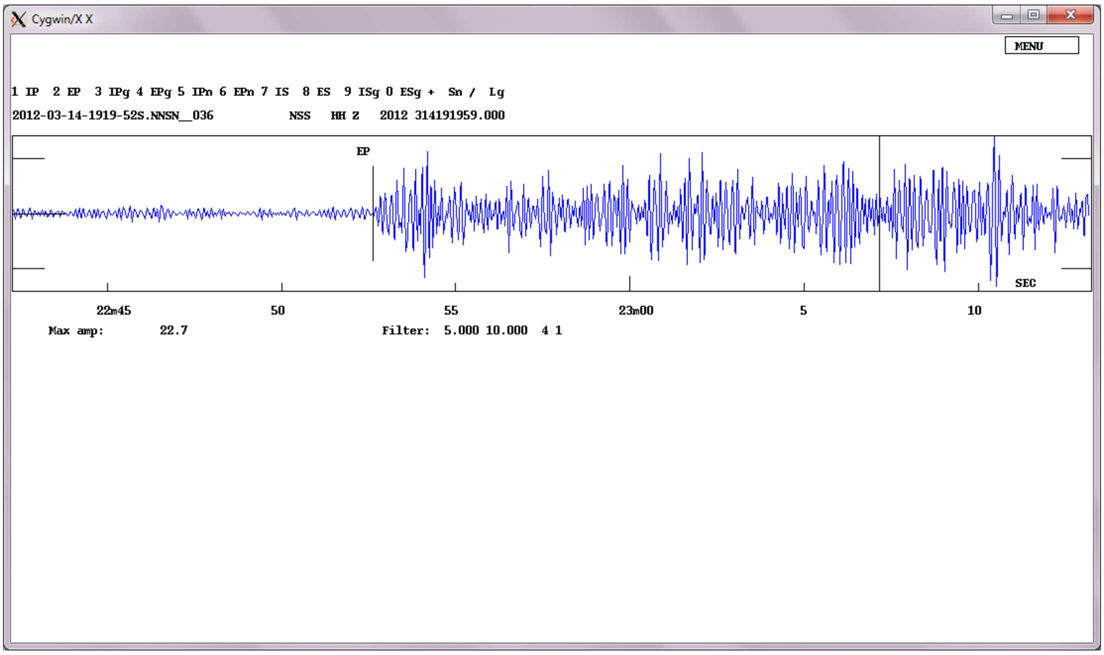

Single-trace plot of station NSS at epicentral distance of 649 km, filtered 5-10 Hz: Going to larger distances, the P arrival becomes more emergent and would not be read without applying a filter.

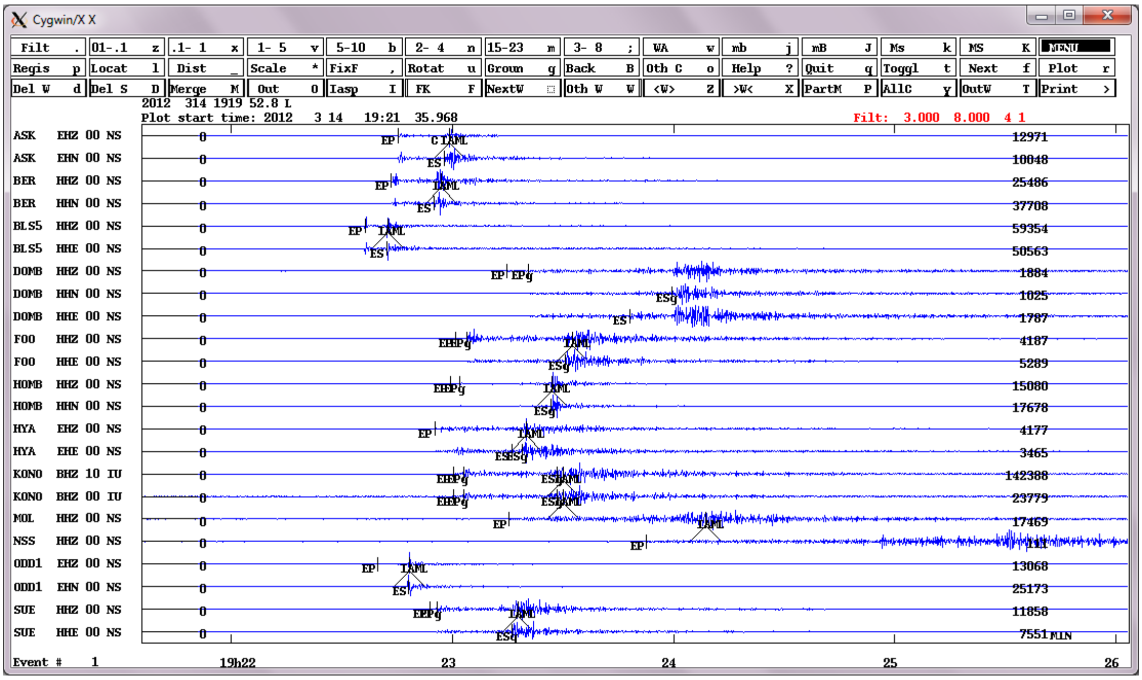

Multi-trace plot of all picked channels: At the end we look at all traces with phase onset and amplitude readings to see whether they are consistently picked. We then start locating. Note that there are simple rules of thumb for a first rough estimates of the approximate hypocenter distance, d, from identified first onsets of P and S waves. If these are Pg and Sg, then it holds d[in km] = (Sg-Pg)[in s] × 8 and in the case of Pn and Sn d = (Sn-Pn) × 10. More accurately, the multiplication factor depends on the average P and S wave crustal velocities [see eq. (3) in EX 11.1]: d = t($S_g - P_g$) (v_p v_s)/($v_p - v_s$).

```
#    1 14 Mar 2012 19:22 28  L  59.526   5.615 13.9    0.4 3.4LBER   12  ? 1

  date hrmn   sec      lat      long depth   no m    rms  damp erln erlt erdp
12 314 1922 28.19 5931.58N   5 36.9E  13.9   29 3   0.36 0.000  4.7  2.0  3.6
 stn   dist   azm  ain w phas    calcphs hrmn tsec  t-obs  t-cal    res   wt di
 BLS5    49 103.3 96.7 0 S       SG      1922 42.3  14.14  14.18  -0.04 1.00  7
 BLS5    49 103.3 96.7 0 P     D PG      1922 36.4   8.15   8.15   0.00 1.00  4
 BLS5    49 103.3      0 IAML            1922 42.5   14.3
 BLS5    49 103.3      0 AMPG            1922 36.4    8.2
 BLS5    49 103.3      0 AMSG            1922 42.4   14.2
 ODD1    71  52.6 93.0 0 S       SG      1922 48.0  19.81  20.02  -0.21 1.00 10
 ODD1    71  52.6 93.0 0 P     D PG      1922 39.8  11.54  11.51   0.04 1.00  1
 ODD1    71  52.6      0 IAML            1922 48.3   20.1
 BER     97 350.7 91.8 0 S       SG      1922 55.0  26.75  26.70   0.05 1.00  4
 BER     97 350.7 91.8 0 P     C PG      1922 43.4  15.22  15.35  -0.12 1.00  2
 BER     97 350.7      0 IAML            1922 56.9   28.7
 ASK    109 347.7 91.5 0 S       SG      1922 57.7  29.52  29.95  -0.43 0.98* 4
 ASK    109 347.7 91.5 0 P     C PG      1922 45.3  17.06  17.21  -0.15 0.98* 3
 ASK    109 347.7      0 IAML            1922 59.4   31.2
 SUE    177 344.9 90.8 0 Sg      SG      1923 16.2  48.02  47.82   0.20 0.87* 3
 SUE    177 344.9 55.1 0 P     C PN4     1922 53.8  25.56  25.93  -0.37 0.87* 4
 SUE    177 344.9 90.8 0 Pg    D PG      1922 55.8  27.61  27.49   0.13 0.87* 2
 SUE    177 344.9      0 IAML            1923 17.7   49.5
 HYA    185   9.4 55.1 0 S       SN4     1923 16.1  47.86  46.91   0.95 0.86*10
 HYA    185   9.4 90.7 0 Sg      SG      1923 19.0  50.78  50.00   0.78 0.86* 3
 HYA    185   9.4 55.1 0 P     C PN4     1922 55.3  27.11  26.96   0.15 0.86* 2
 HYA    185   9.4      0 IAML            1923 20.1   51.9
 HYA    185   9.4 90.7 0 Pg      PG      1922 57.1  28.85  28.74   0.12 0.86* 0
 HOMB   217 128.8 90.6 0 Sg      SG      1923 26.8  58.57  58.49   0.08 0.80* 6
 HOMB   217 128.8 90.6 0 Pg    C PG      1923  2.1  33.86  33.62   0.25 0.80* 4
 HOMB   217 128.8      0 IAML            1923 27.2   59.0
 HOMB   217 128.8 55.1 0 P     C PN4     1922 59.4  31.24  30.96   0.28 0.80* 6
 KONO   225  84.8 55.1 0 P       PN4     1923  0.3  32.12  31.95   0.17 0.79* 3
 KONO   225  84.8 90.6 0 Pg    D PG      1923  2.9  34.70  34.81  -0.11 0.79* 1
 KONO   225  84.8 90.6 0 Sg      SG      1923 28.5  60.31  60.58  -0.26 0.79* 5
 KONO   225  84.8      0 IAML            1923 30.2   62.0
 FOO    233 352.5 90.6 0 Sg      SG      1923 30.7  62.45  62.57  -0.12 0.78* 2
 FOO    233 352.5 55.1 0 P       PN4     1923  0.9  32.71  32.88  -0.17 0.78* 2
 FOO    233 352.5 90.6 0 Pg      PG      1923  3.9  35.69  35.96  -0.27 0.78* 1
 FOO    233 352.5      0 IAML            1923 32.5   64.3
 DOMB   342  32.3 55.1 0 S       SN4     1923 48.1  79.93  80.82  -0.89 0.60* 6
 DOMB   342  32.3 90.4 0 Sg      SG      1923 59.5  91.25  91.28  -0.03 0.60* 3
 DOMB   342  32.3 55.1 0 P     C PN4     1923 14.9  46.70  46.45   0.26 0.60* 1
 DOMB   342  32.3 90.4 0 Pg      PG      1923 20.6  52.35  52.46  -0.11 0.60* 0
 MOL    355  16.3 55.1 0 P       PN4     1923 15.4  47.23  48.03  -0.80 0.57* 1
 MOL    355  16.3      0 IAML            1924  8.9  100.7
 NSS    649  28.0 53.1 0 P       PN5     1923 52.6  84.43  83.82   0.61 0.08* 0
 ODD1 EZ   hdist:      72.6   amp:       4529.1 T:   0.4   ml =   3.7
 BER  HZ   hdist:      97.8   amp:       1863.0 T:   0.4   ml =   3.5
 ASK  EZ   hdist:     109.9   amp:       2311.9 T:   0.1   ml =   3.6
 SUE  HZ   hdist:     177.5   amp:       1124.8 T:   0.1   ml =   3.6
 HYA  EZ   hdist:     185.5   amp:        629.6 T:   0.4   ml =   3.4
 HOMB HZ   hdist:     218.4   amp:       1355.1 T:   0.4   ml =   3.8
 KONO BZ   hdist:     225.4   amp:        144.8 T:   0.2   ml =   2.8
 MOL  HZ   hdist:     355.3   amp:        112.3 T:   0.1   ml =   3.0
 FOO  HZ   hdist:     233.4   amp:        388.3 T:   0.4   ml =   3.3
 BLS5 HZ   hdist:      50.9   amp:       6142.4 T:   0.1   ml =   3.7
 BLS5 HZ   gdist:      50.9   mom:          13.5   mw =   2.9
 FOO  HZ   gdist:     231.4   mom:          13.6   mw =   3.0
 Number of spectra available and number used in average     2     2
 2012  314 1922 28.2 L  59.526   5.615 13.9  BER 12 0.4 3.4LBER 3.0WBER
```

Output from location program: We use a standard linearized inversion program (HYPOCENTER, Lienert et al. (1986, 1995)) to locate the event that makes use of the common seismic phases at local distances. The location program tries to minimize the differences between the observed (t-obs) and calculated arrival times (t-cal) that are computed for a 1D layered model. The residuals are given in the column labeled 'res'. For our example event these travel-time residuals are relatively small. Note that for station DOMB the residuals are given for both Pn/Pg and Sn/Sg and that our interpretation fits the solution.

Direct (Pg and Sg) and critically refracted wave types (Pn and Sn) were very clearly visible from this earthquake on the records of several stations. This helped to constrain the earthquake depth, which was estimated to be 13.9 km (see last but one line). At the end the location procedure the program gives the magnitude values for the individual components and stations, and calculates the average, which is 3.4 in this case. The text ‘LBER’ refers to the magnitude type (L for ML) and the reporting agency (BER = Bergen). Some spread in the magnitude residuals (difference between single-component magnitude and average) is expected and mostly due to local site effects. In our case the largest residual are -0.6 and +0.4 magnitude units.

A number of polarities were read, 7 compressional (C) and 4 dilatational (D), which are given in the column after the phase name read and the phase used by the location program. For example, in the second phase line of the location output for stations BLS5, the first phase arrival was read as P, the location program decides that this is the direct Pg arrival based on the hypocentral distance. The polarity is read as D, standing for down or dilatation. The location program computes the azimuth (azm) and angle of incidence (ain), which in this example are 103.3° and 96.7°, respectively. The polarity data can be used to determine the fault plane solution if there are sufficient observations. In this example we can not find a robust solution and do not show the procedure here.

The velocity model used is given by the following table:

Depth of top of layer in km	*P-wave velocity in km/s*
0	6.2
12	6.6
23	7.1
31	8.05
50	8.25
80	8.5

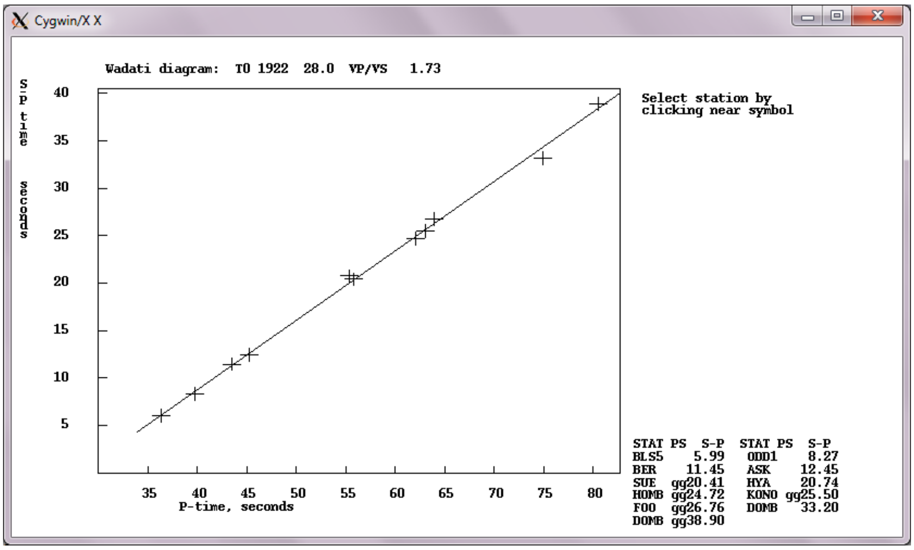

Wadati diagram: To check our readings we can plot the Wadati diagram (plotting S-P times against absolute P arrival times (labels on x-axis given to show scaling), and the data points should fall onto a line like in this example. Data points (+) that are significantly off the line should be checked and re-read.

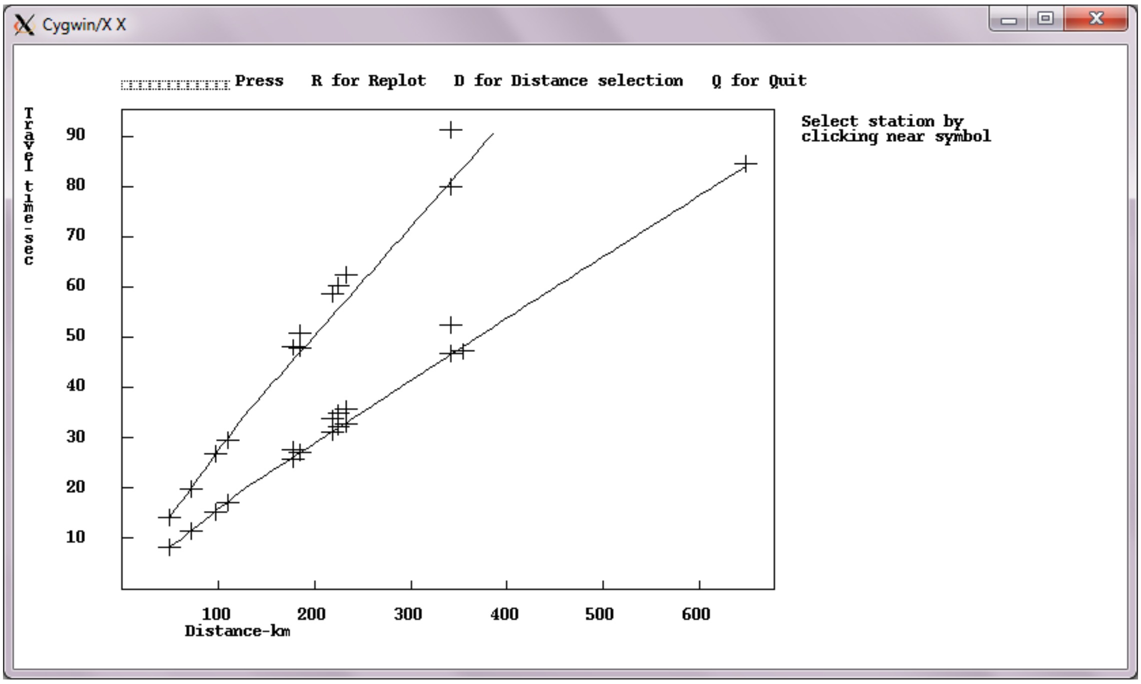

Travel time plot: We can also produce a simple travel-time plot that shows the observations (+) together with the calculated travel-time curves for P and S first arrivals according to the local velocity model implemented in the SEISAN location program (solid lines). For distances greater than about 150 km, our Pg (around the lower curve) and Sg arrivals (around the upper curve) come in mostly after the predicted first arrivals.

Note that SEISAN uses layered 1D velocity models and the user needs to enter the model for his or her respective area. SEISAN allows the use of a number of 1D models for events depending on their location to account for changes in structure within the area of interest or network coverage.

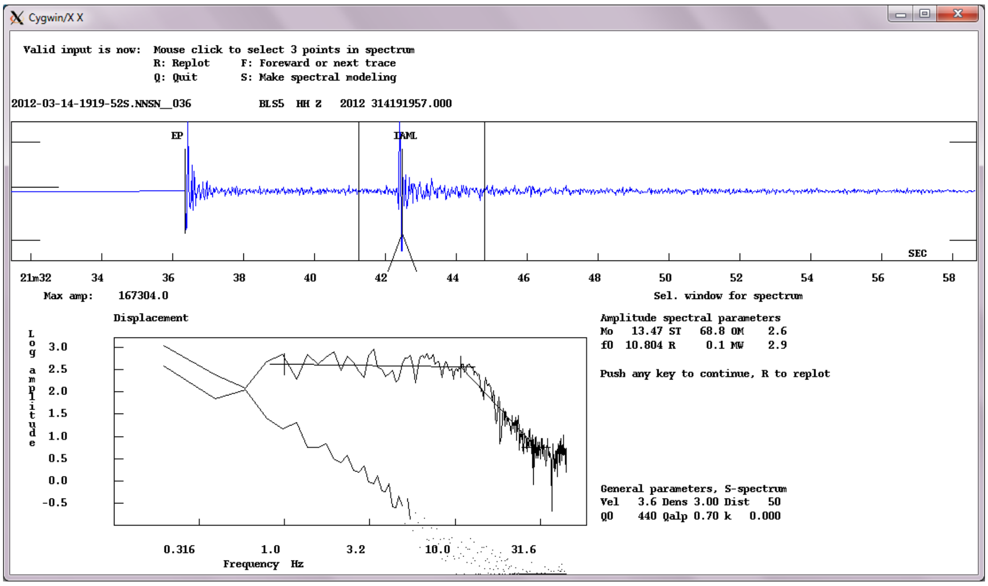

Source spectrum plot for station BLS5 at epicentral distance of 49 km: We compute the source displacement spectrum (upper curve in the bottom diagram above the noise spectrum) for the vertical component of this station. The spectrum is corrected for attenuation, which for Norway is given by $Q(f) = 440 \times f^{0.7}$ (see data at bottom right). From the spectrum we can approximately read the long-period spectral level, which is translated via the assumed velocity and density model into seismic moment (here $\log_{10}M_0 = 13.47$ Nm) and moment magnitude ($M_W = 2.9$). We also measure the corner frequency ($f_c = 10.8$ Hz), which is translated into stress drop $\Delta\sigma = 68.8$ bars = 6.88 MPa using $\Delta\sigma = (7/16)\, M_0/R^3$ (Eshelby, 1957).

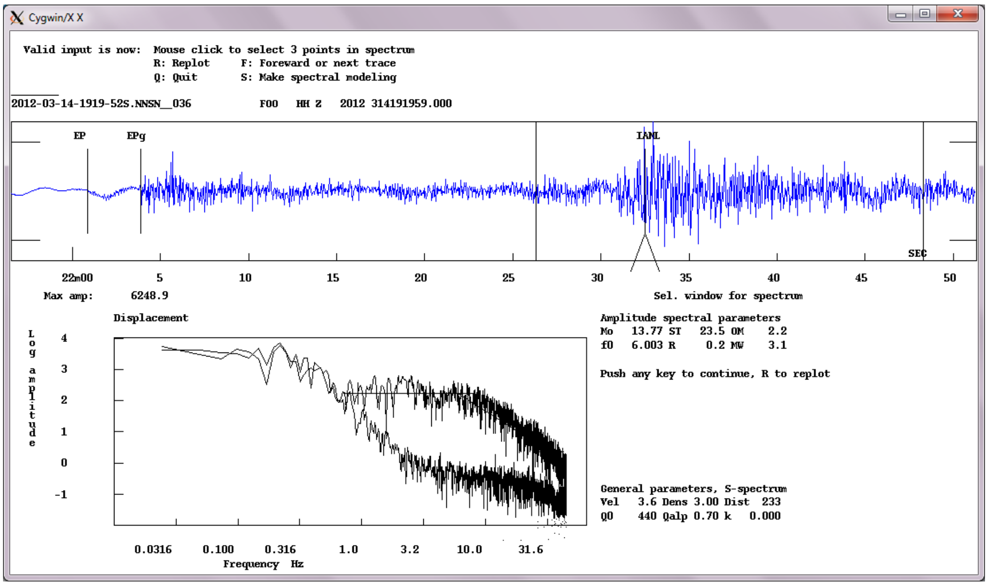

Source spectrum plot for station FOO at epicentral distance of 233 km: The spectral analysis is normally done for a number of stations with good SNR. When comparing the results for this station with those of the previous station (BLS5) one finds the difference between the moment magnitudes to be small, but the stress drop difference to be large because of the reading uncertainty in f_c and $\Delta\sigma \sim f_c^3$. (For related formulas and discussions see EX 3.4). At the end, the averages are computed from all observations and standard deviations are calculated.

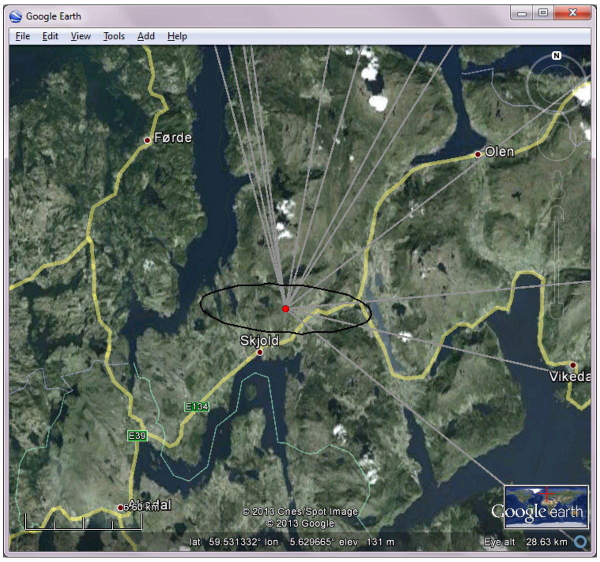

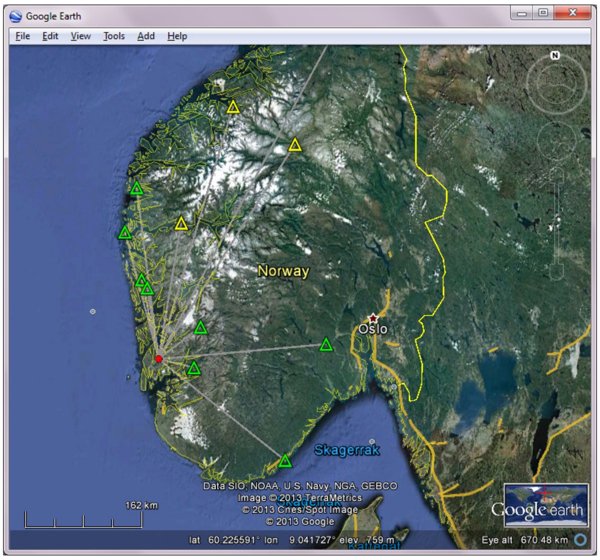

Location maps in GoogleEarth: SEISAN creates files that make it possible to look at the location with GoogleEarth immediately. The figure on the left shows the epicenter area with the error ellipse plotted as a solid black line. The extent of the 90 percent confidence error ellipse is about 2.5 by 9.0 km. It is also possible to compare the epicenter location to known fault structures. In the case of explosions we try to see if the event is located close to a known mine or quarry.

On the right, we show a more regional GoogleEarth map, which shows the epicenter as a red dot. The stations are color coded depending on their residual from the hypocenter location where green is low residual, yellow is moderate residual and red is high residual (the color levels are configurable). In this example, there are no stations towards the west and southwest of the epicenter and stations are sparse toward the southeast, resulting in an azimuthal gap of 216 degree. This, together with the dominating N-S extension of the Norwegian network causes the much larger location uncertainty in E-W direction (see error ellipse in the left-hand panel). We can also plot the epicenter together with previously located earthquakes.

3 Analysis of a regional earthquake recorded at distance between 440 and 2950 km (Δ < 30°)

As an example we have chosen an earthquake that occurred on the Mohns Ridge, offshore northern Norway. The earthquake with a magnitude greater than 6 was large enough to be recorded globally. Here, we process data that were recorded on the Norwegian National Seismic Network operated by the University of Bergen and data provided by IRIS from the Global Seismograph Network (GSN). All data used here was recorded on broadband stations.

The earthquake parameters provided by the USGS are:

Date:	24 May 2012
Origin time:	22:47:46.6 (UTC)
Latitude:	72.99°N
Longitude:	5.65°E
Depth:	8.8 km
Mw:	6.2

We now show the step-by-step procedure to analyze the earthquake.

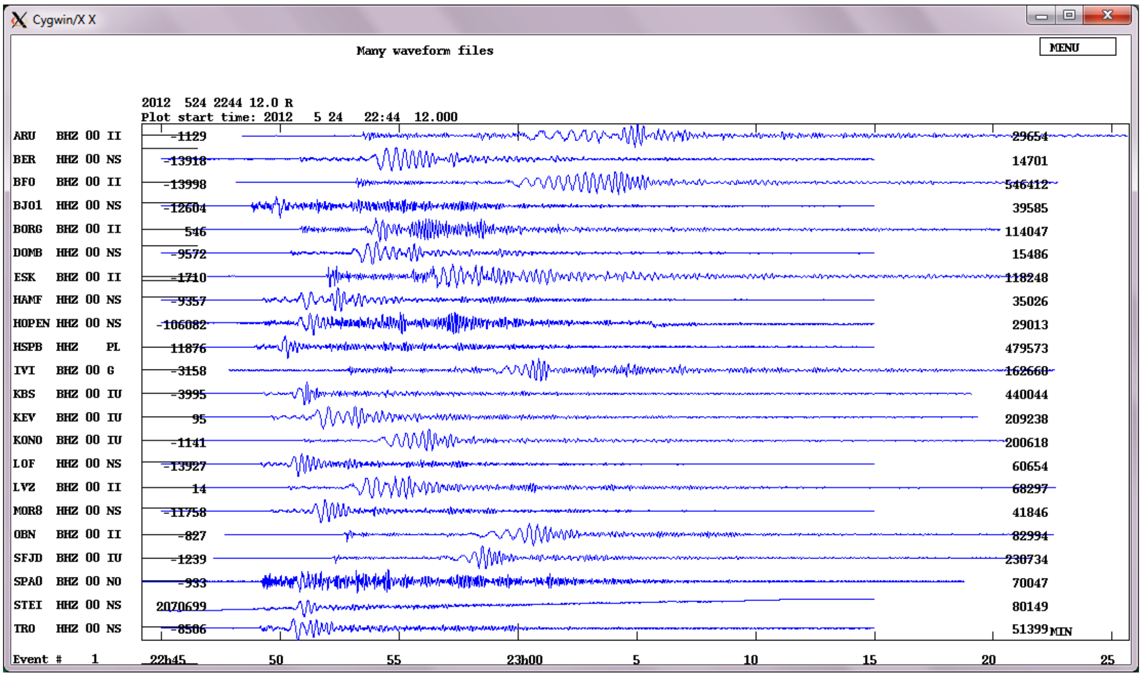

Vertical component multi-trace plot, unfiltered: On the seismograms we clearly see long-period surface waves, with large amplitudes and pronounced dispersion. This indicates that the earthquake is relatively large and shallow. For the stations, where we see the first arriving P as well we can estimate the approximate distance from the time difference between the P and the Rayleigh surface wave maximum (which is most pronounced in vertical component records). For station BFO this time difference is about 10 min. According to Table 1 below this means that station BFO is about 20 to 25° degrees away (1° = 111.2 km) from the epicenter. Being aware of the station locations, considering the pattern of arrival times, and, if three-component records are available, also of the first-motion polarity patterns and the better constraining S-P travel-time differences, we can also get a first guess of the epicenter location (see EX 11.2).

Table Approximate time interval (t_{Rmax} - t_P) between the arrival of the maximum Rayleigh wave amplitude and the first onset of P waves as a function of epicentral distance Δ according to Archangelskaya (1959) and Gorbunova and Kondorskaya (1977) for dominatingly continental travel paths.

Δ°	t_{Rmax} - t_P (min)	Δ°	t_{Rmax} - t_P (min)	Δ°	t_{Rmax} - t_P (min)
10	4-5	55	26	100	45-46
15	6-8	60	28-29	105	47-48
20	9-10	65	31	110	48-50
25	10-12	70	33	115	53
30	13-14	75	35	120	55
35	15-16	80	37	125	57
40	18-19	85	39-40	130	60
45	21	90	42	140	64
50	24	95	43	150	70

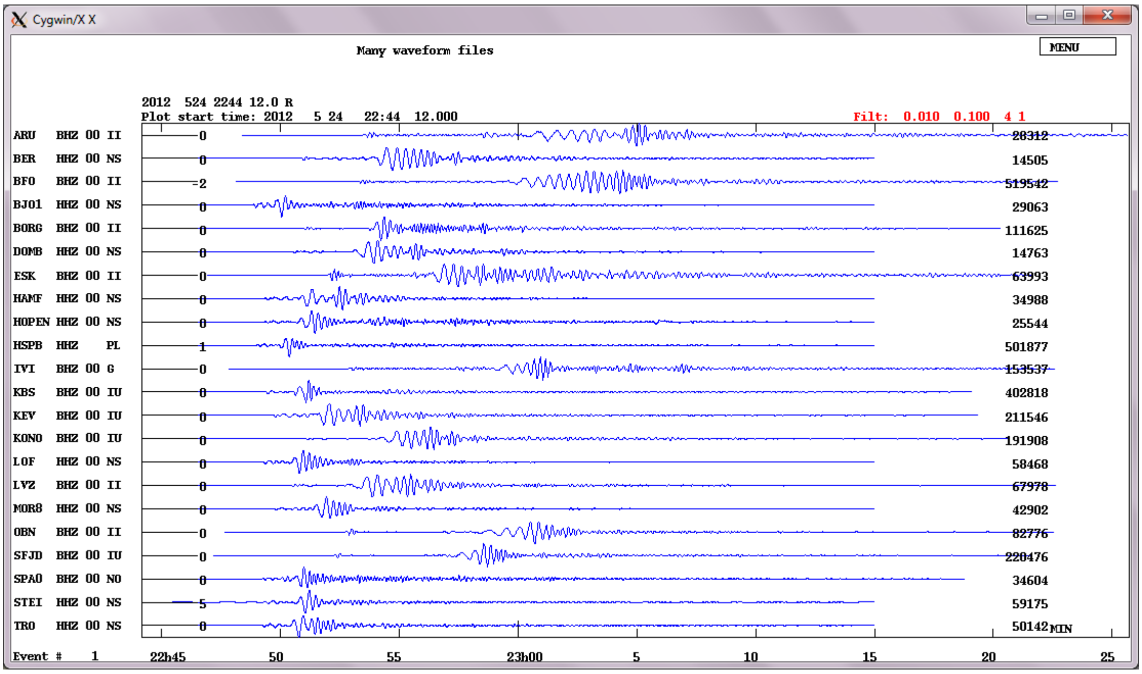

Vertical component multi-trace plot, filtered 0.01-0.1 Hz: Filtering the data at low frequencies, we see both body and surface waves. However, the seismograms are dominated by the surface waves as they have larger amplitudes in this frequency range. The shape of the surface wave trains depends on the Earth structure along the paths (see, e.g., Chapter 2, Figs. 2.10, 2.12 and 2.13) and, because of the dispersion, i.e., the dependence of the surface-wave velocity on the period, also on the epicentral distance (see Figure above). The seismograms also depend on the mechanism of faulting.

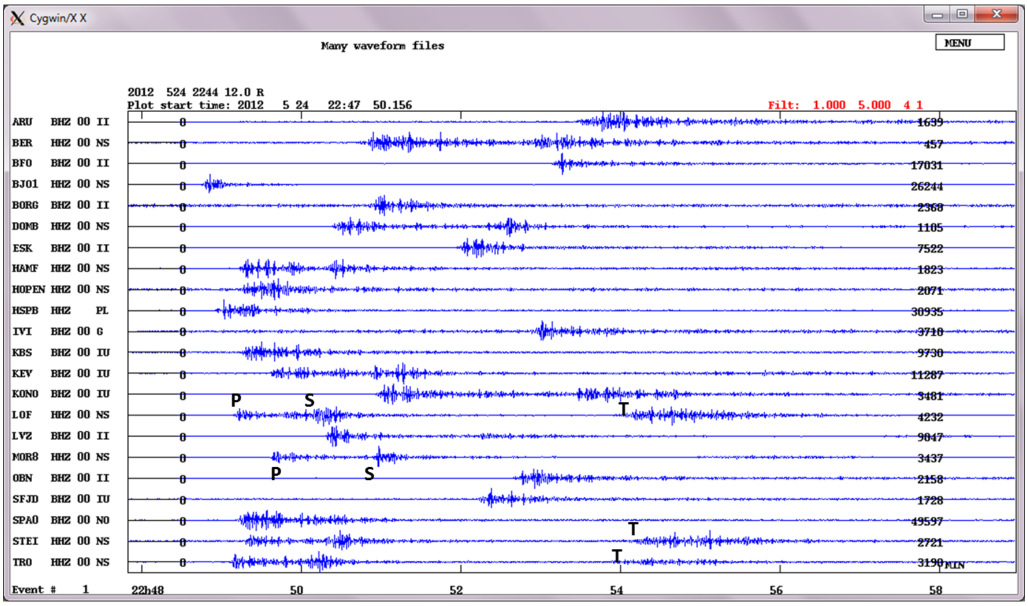

Multi-trace plot, filtered 1-5 Hz: Looking at higher frequencies, the surface waves disappear from the seismogram and we look at P and (at these high frequencies and in vertical component records usually less clear) S body waves. If the first arriving P and S phases are Pn and Sn, respectively, then there is a simple "rule of thumb" to estimate the hypocenter distance, namely time difference Sn-Pn [in s] × 10. For station LOF with a time difference of about 1 min this means a distance of ≈ 600 km, This agrees with the rough estimate from the time difference between the Rayleigh-wave maximum and the P first arrival. On some stations (STEI, TRO and LOF) we can also see a signal in this frequency range arriving much later (about 5 minutes after P for station TRO). This is the T(tertiary)-wave, generated by an earthquake in or near the oceans, propagating in the oceans as an acoustic wave and converted back to seismic wave at the ocean-land boundary near the recording site. (for more explanations see Chapter 2, section 2.6.5). It should not be mistaken for another event.

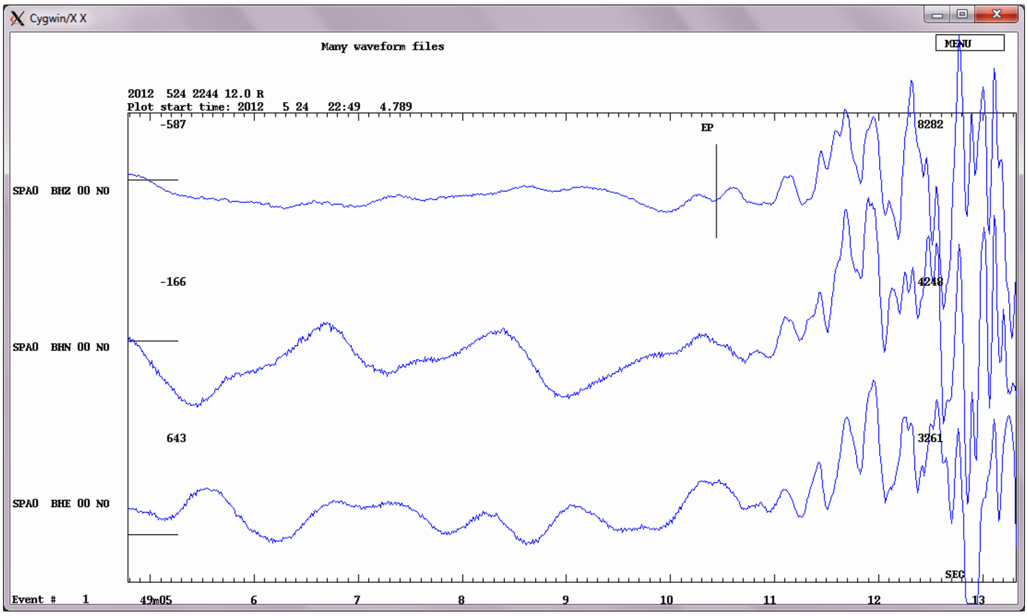

Three-component traces of station SPA0 at epicentral distance of 648 km, unfiltered: Zooming around the P arrival the phase can be picked with or without filter. The error on the phase reading here may be as large as 0.5 sec.

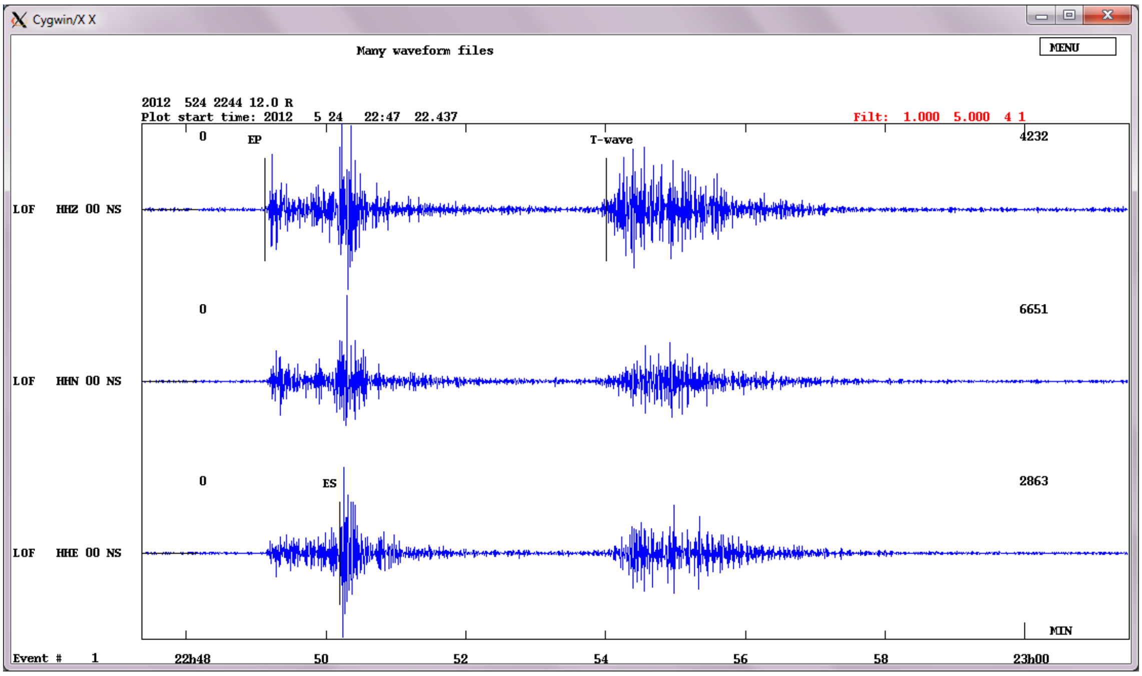

Three-component traces of station LOF at epicentral distance of 603 km, filtered 1-5 Hz: Looking at this coastal station, we clearly see the arrival of the T wave. The amplitude of the T wave is in this case comparable to the S-wave amplitude. According to the time difference (S-P)[in s]×10 the station is about 600 km away from the source.

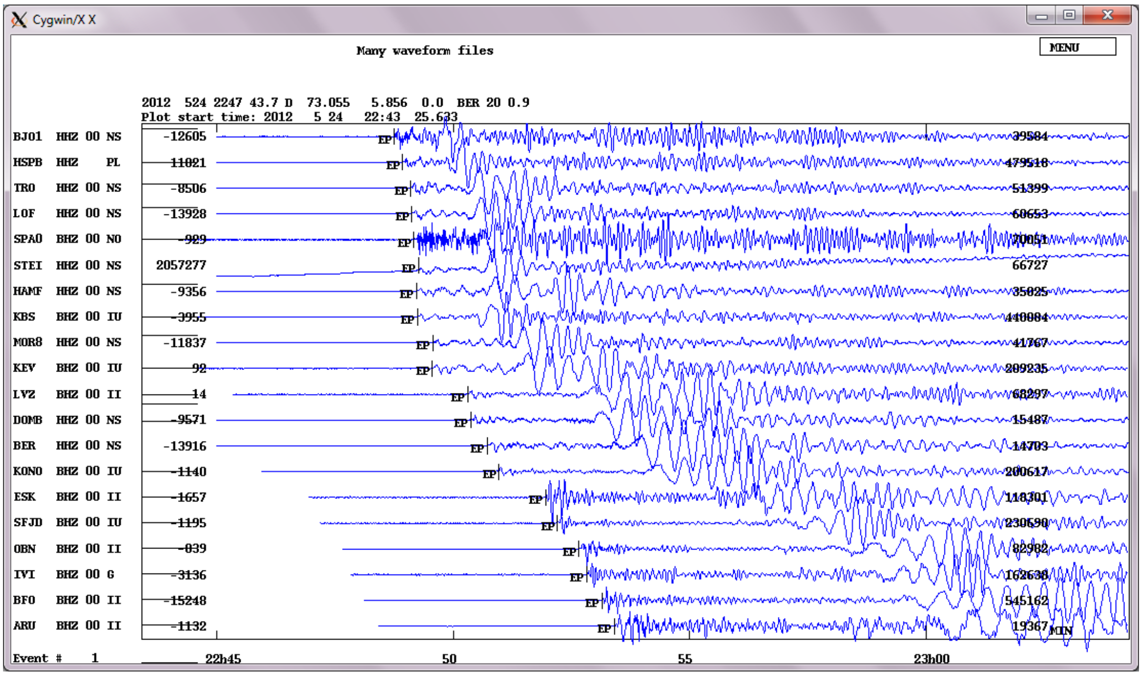

All vertical traces, unfiltered: The traces are sorted by distances and the P arrival picks are shown. This type of plot is useful to check the consistency of the picks. Based on the P arrival times, the epicenter is estimated at 73.055°N and 5.856°E. The hypocenter depth is not constrained by the data and given as 0 km by the location program. On stations like SPA0 we can see that we have both high and low frequency. Towards larger distances the high frequencies get attenuated more strongly than lower frequency signals.

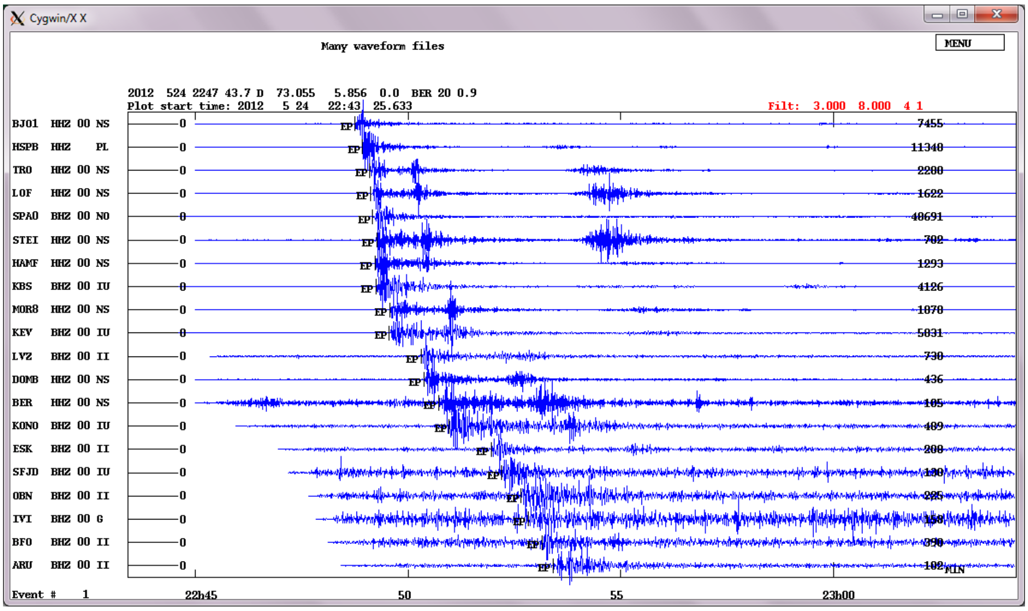

All vertical traces, filtered 3-8 Hz: We can see that the signal amplitude of the higher frequencies decreases as we go to larger distances due to attenuation. The distance range here is approximately 440 km (station BJO1) to 2960 km (station ARU).

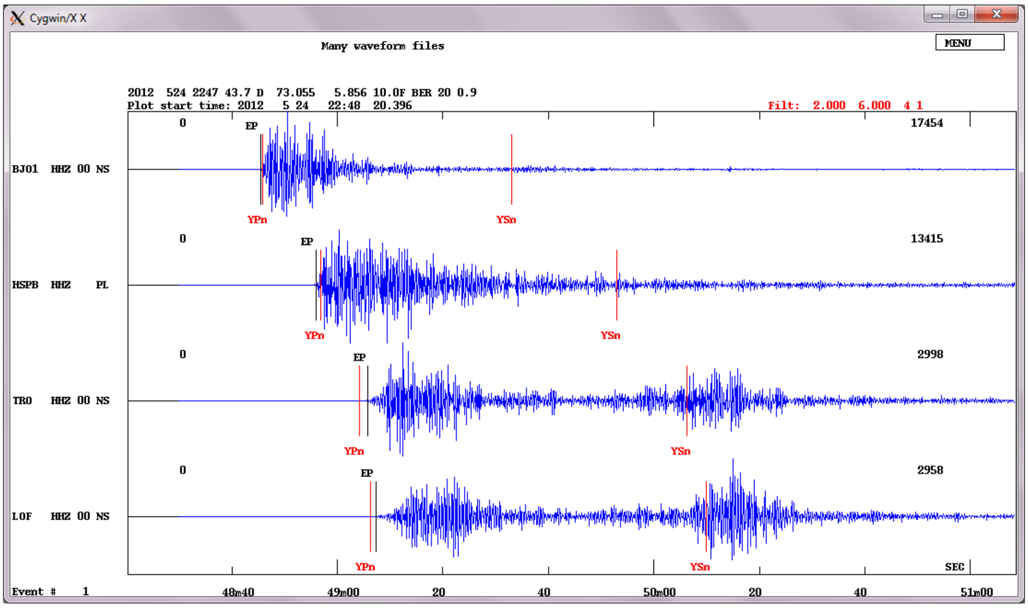

Selected vertical traces, filtered 2-6 Hz: Computed Pn and Sn phase arrival times have been marked by red vertical lines and the text 'yPn' and 'ySn'. No S-waves are recognizable in the records of the two stations BJO1 and HSPB closer to the epicenter. They are likely situated in an azimuth range of minimum S-wave and strong P-wave radiation (see EX 3.2). While S appears at larger distances, the phase is emergent and from this plot its travel-time does not match well with the global velocity model used (IASP91). The earthquake is located on the Mid-Atlantic Ridge. The seismograms are complicated both due to source and path effects, including the transition from oceanic to continental crust. The display of theoretical arrivals should only serve as a guide on whether the considered phase is plausible to arrive in this time window. However, it would be **wrong** to pick a phase close to the predicted time if there is no visible change in the signal.

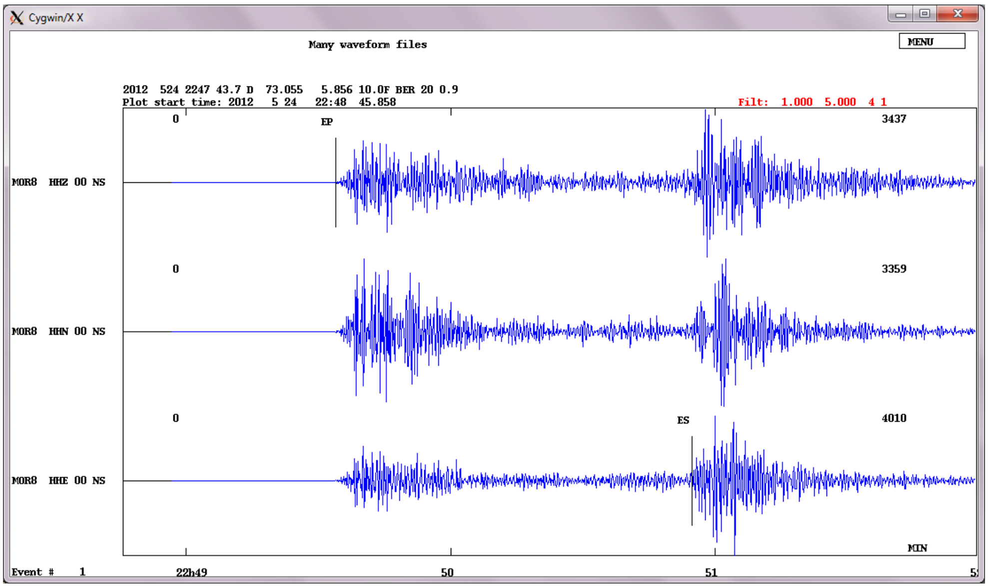

Three-component trace plot of station MOR8 at epicentral distance of 813 km, filtered 1-5 Hz: This is an example where the S arrival can be read quite well on one of the horizontal channels.

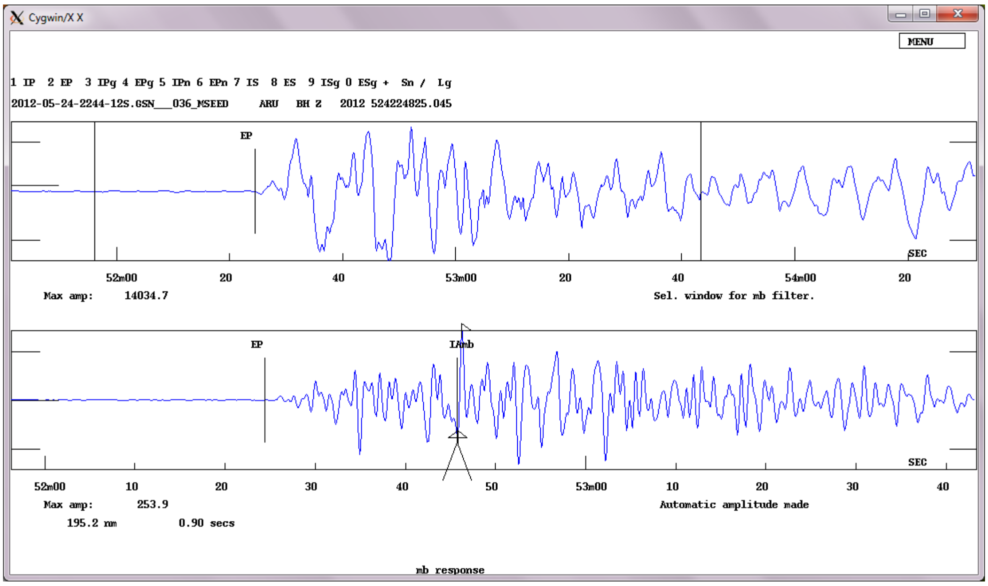

Vertical-component trace of station ARU (Δ=26.7°), mb filter: While it is possible to read ML amplitudes from this earthquake for stations within about 1500 km, this is not done because the ML scale for Norway is not appropriate for sources on the Mid-Atlantic Ridge. We, therefore, read amplitudes for the teleseismic magnitudes which can be used down to distances of 20° and even down to 2° for standard Ms_BB. Moment magnitude for this event can be measured using either regional or teleseismic moment tensor inversion (USGS Mw = 6.2). The plot above shows the mb amplitude reading for station ARU. This is done by deconvolving the broadband instrument response and applying a filter to simulate the WWSSN short-period seismograph (see IS 3.3). The simulation trace is displayed on the bottom trace for the time window indicated by the vertical lines on the top trace (raw data). The amplitude IAmb is automatically read between the largest peak and adjacent trough. It is stored as half of this measurement, which is 195.2 nm, together with the related period T of 0.90 s which is twice the time difference between peak and trough.

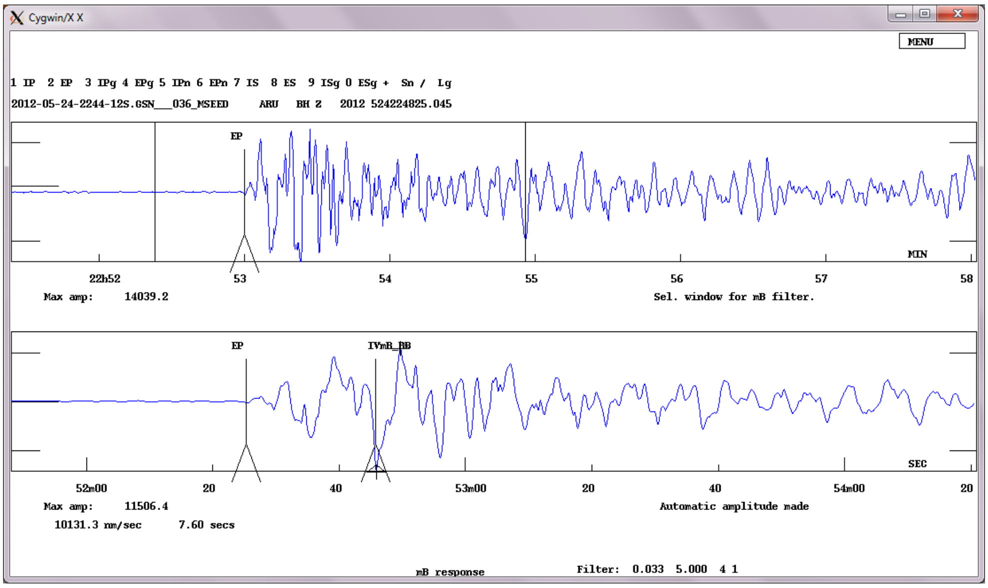

Vertical-component trace of station ARU (Δ=26.7°), mB_BB filter: This plot shows the mB_BB amplitude reading made for station ARU. This is done by deconvolving the actual instrument response to a broadband velocity response and reading the velocity amplitude on the simulation trace which is displayed on the bottom for the time window indicated by the vertical lines on the top trace (raw data). The amplitude is automatically read between peak and trough, and stored as half of this measurement, which is 10131.3 nm/s with a period of 7.60 s. The period for mB_BB needs to be within 0.2 s < T < 30 s (see IS 3.3).

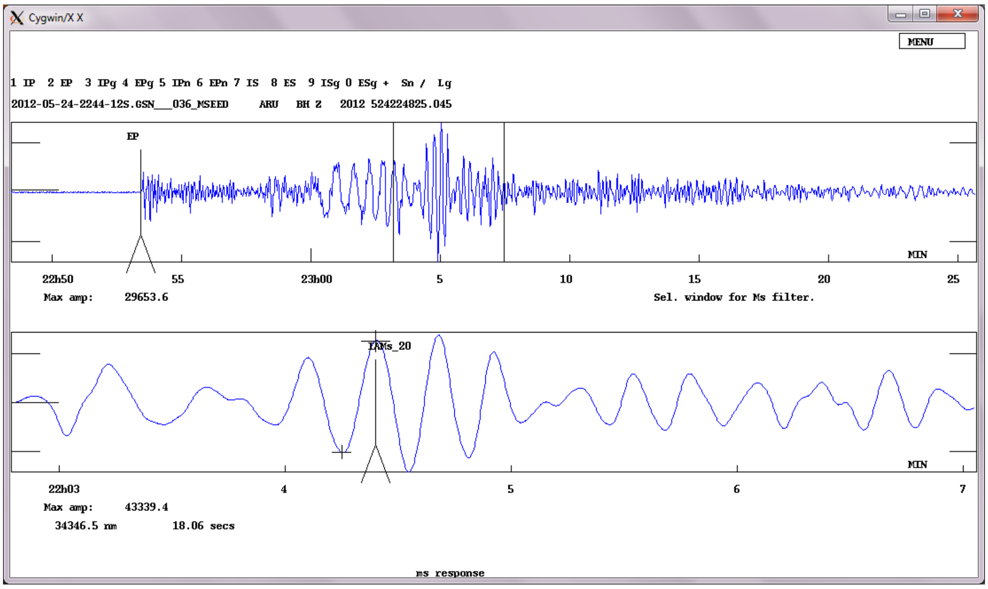

Vertical-component trace of station ARU (Δ=26.7°), Ms_20 filter: This plot shows the Ms_20 amplitude reading made for station ARU. This is done by deconvolving the displacement instrument response and applying a filter to simulate the WWSSN long-period seismograph. The simulation trace is displayed on the bottom for the time window indicated by the vertical lines on the top trace (raw data). The amplitude is automatically read between peak and trough, and stored as half of this measurement, which is 34346.5 nm with a period of 18.06 s. The period for Ms_20 needs to be within 18 s ≤ T ≤ 22 s.

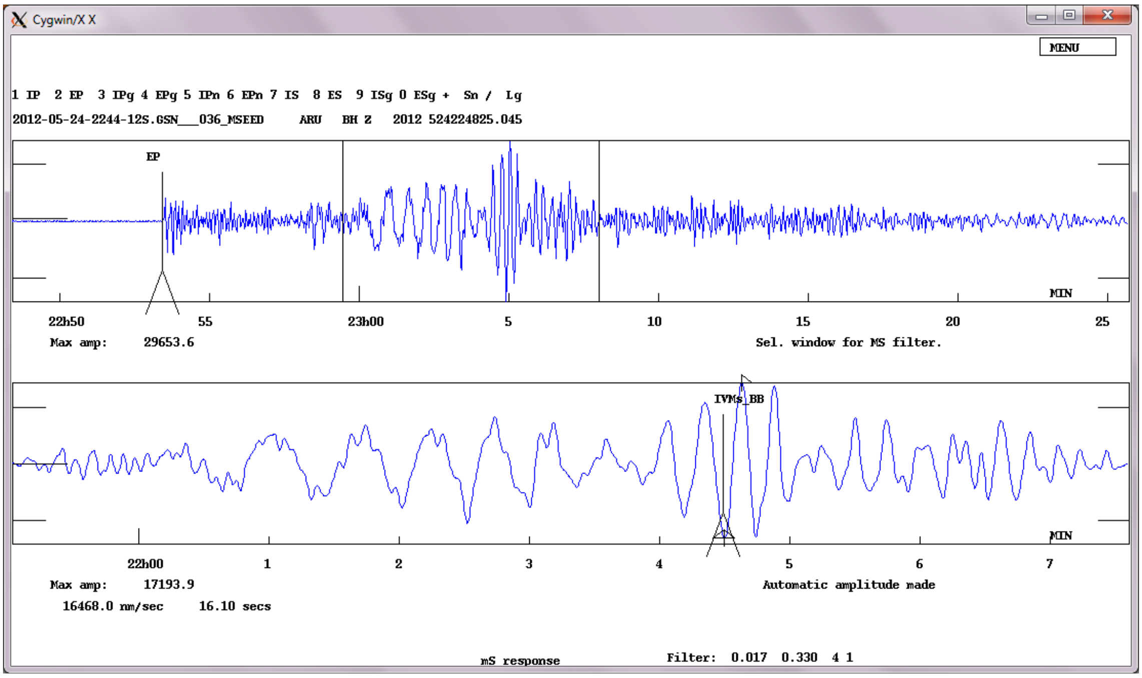

Vertical-component trace of station ARU (Δ = 26.7°), Ms_BB filter: This plot shows the Ms_BB amplitude reading made for station ARU. If the primary record is not yet a velocity broadband trace then the latter has to be synthesized by deconvolving the actual instrument response to a broadband velocity response and reading the velocity amplitude on the simulation trace. The latter is displayed on the bottom trace for the time window indicated by the vertical lines on the top trace (raw data). The amplitude is automatically read between the largest peak and adjacent trough, and stored as half of this measurement, which is 16468.0 nm/s, together with a period of 16.10 s, i.e., twice the time difference between the peak and adjacent trough. The period needs to be within 3 s ≤ T ≤ 60 s, and thus maybe significantly shorter than for Ms_20 measurement, allowing Ms measurements at distances well below 20° (down to 2°).

Based on these four amplitude and period measurements from station ARU, we can compare the magnitudes to Mw:

Magnitude scale	**Value**
Mw (USGS)	6.2
mb	5.9
mB_BB	6.7
Ms_20	6.0
Ms_BB	6.1

We see that the values for this size of earthquake around magnitude 6 compare well, with the exception of mB_BB which is on global average about 0.3 -0.4 m.u. greater than Mw at Mw = 6.2 and about 0.6 m.u larger than mb.

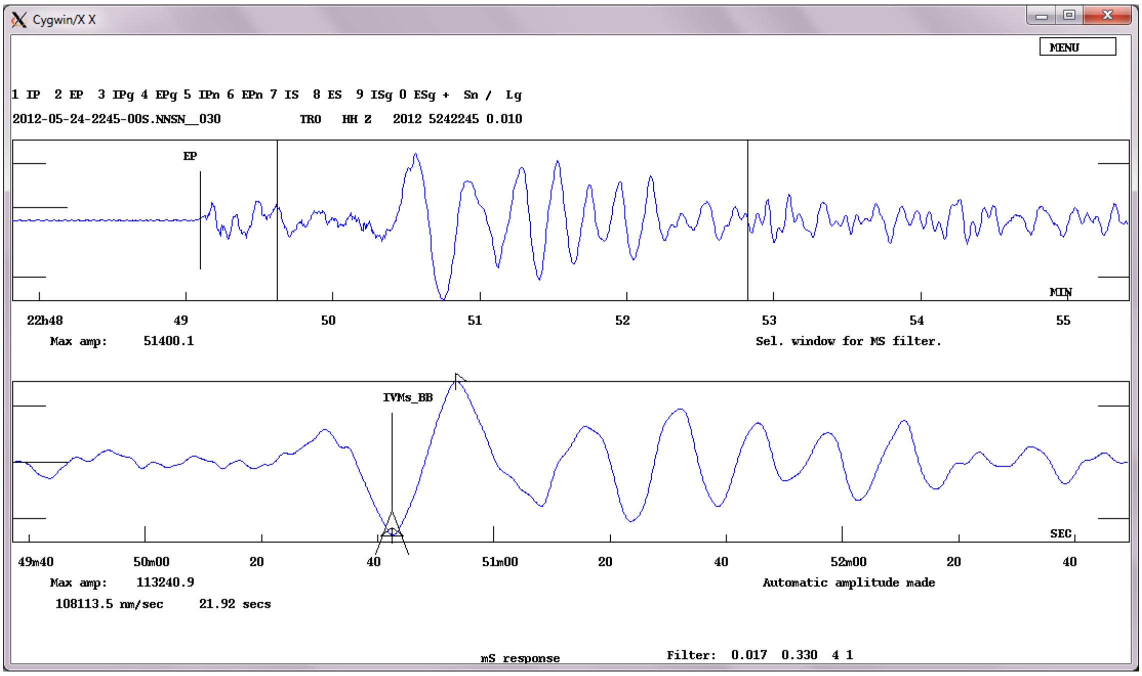

Vertical-component trace of station TRO at Δ=5.3°, Ms_BB filter: Ms_BB can be used down to distances of 2°. This plot shows the Ms_BB amplitude reading made for station TRO. The amplitude is automatically read between peak and trough, and stored as half of this measurement, which is 108113.5 nm/s with a period of 21.92 s. The computed magnitude is Ms_BB = 5.7, compared to Ms_BB = 6.1 for station ARU.

```
#    1 24 May 2012 22:47 45  D  72.943   6.096  8.8F   1.8 6.3sBER   20  ? 1

  date hrmn   sec      lat      long depth   no m    rms  damp erln erlt erdp
12 524 2247 45.09 7256.61N   6  5.7E   8.8*  24 2   1.77 0.000 47.0  9.2  0.0
 stn   dist   azm  ain w phas    calcphs hrmn tsec  t-obs  t-cal    res   wt di
 BJO1   439  60.6 45.8 0 P       Pn      2248 45.4  60.36  60.82  -0.46 1.00  6
 HSPB   528  26.6 45.8 0 P       Pn      2248 56.0  70.88  71.85  -0.97 1.00  7
 TRO    587 122.6 45.8 0 P       Pn      2249  5.8  80.70  79.19   1.51 1.00  1
 TRO    587 122.6      0 IVMs_BB         2250 42.4  177.3
 LOF    603 149.2 45.8 0 P       Pn      2249  7.4  82.27  81.18   1.09 1.00  1
 LOF    603 149.2 48.3 0 S       Sn      2250  6.4 141.35 144.88  -3.53 1.00  5
 SPA0   648  21.2 45.8 0 P       Pn      2249 10.4  85.35  86.84  -1.49 1.00  7
 STEI   654 144.2 45.8 0 P       Pn      2249 15.7  90.63  87.49   3.14 1.00  1
 STEI   654 144.2 48.2 0 S       Sn      2250 18.9 153.78 156.21  -2.43 1.00  6
 HAMF   662 104.2 45.8 0 P       Pn      2249 13.8  88.70  88.50   0.20 1.00  3
 KBS    685  10.5 45.8 0 P       Pn      2249 14.6  89.50  91.27  -1.77 1.00  8
 MOR8   813 151.6 45.7 0 P       Pn      2249 34.0 108.87 107.24   1.63 1.00  1
 MOR8   813 151.6 48.1 0 S       Sn      2250 54.7 189.65 191.69  -2.04 1.00  5
 KEV    821 105.3 45.7 0 P       Pn      2249 33.8 108.76 108.20   0.56 1.00  3
 LVZ   1191 103.8 45.6 0 P       Pn      2250 18.8 153.67 153.99  -0.32 1.00  3
 DOMB  1219 172.5 45.6 0 P       Pn      2250 22.6 157.46 157.34   0.12 1.00  2
 DOMB  1219 172.5 47.8 0 S       Sn      2252 25.0 279.88 281.53  -1.65 1.00  7
 BER   1401 181.7 45.5 0 P       Pn      2250 43.7 178.61 179.70  -1.09 1.00  3
 KONO  1490 172.3 45.4 0 P       Pn      2250 58.2 193.13 190.69   2.44 1.00  2
 ESK   2010 197.3 39.8 0 P       Pn      2251 57.3 252.18 251.84   0.34 1.00  5
 ESK   2010 197.3      0 IVmB_BB         2252  6.0  260.9
 ESK   2010 197.3      0 IAmb            2252 12.8  267.7
 ESK   2010 197.3      0 IAMs_20         2257 17.9  572.8
 SFJD  2172 281.2 34.8 0 P       P       2252 11.8 266.68 267.71  -1.03 1.00 12
 SFJD  2172 281.2      0 IAmb            2252 23.3  278.2
 SFJD  2172 281.2      0 IVMs BB         2258 30.4  645.3
 SFJD  2172 281.2      0 IAMs_20         2258 34.0  648.9
 OBN   2420 128.4 34.0 0 P       P       2252 39.3 294.24 291.96   2.28 1.00  0
 OBN   2420 128.4      0 IVmB_BB         2252 50.0  304.9
 OBN   2420 128.4      0 IAmb            2252 55.4  310.3
 OBN   2420 128.4      0 IAMs_20         23 0 30.7  765.6
 OBN   2420 128.4      0 IVMs_BB         23 0 39.0  773.9
 IVI   2570 268.3 33.4 0 P       P       2252 50.1 304.96 306.21  -1.25 1.00 11
 BFO   2743 176.4 28.4 0 P       P       2253  9.1 324.01 321.15   2.86 1.00  1
 ARU   2954 100.0 28.1 0 P       P       2253 25.2 340.13 338.25   1.87 1.00  1
 ARU   2954 100.0      0 IAmb            2253 45.7  360.6
 ARU   2954 100.0      0 IVmB_BB         2253 45.8  360.7
 ARU   2954 100.0      0 IAMs_20         23 4 49.9 1024.8
 ARU   2954 100.0      0 IVMs_BB         23 4 54.1 1029.0
 TRO  HZ    dist:     587.0   amp:      108000.0 T:  21.9   MS =   5.7
 ESK  BZ    dist:    2010.0   amp:      154000.0 T:   7.1   mB =   7.3
 ESK  BZ    dist:    2010.0   amp:       11890.7 T:   1.8   mb =   6.7
 ESK  BZ    dist:    2010.0   amp:      363000.0 T:  21.6   Ms =   6.6
 SFJD BZ    dist:    2172.0   amp:        4562.0 T:   2.9   mb =   6.2
 SFJD BZ    dist:    2172.0   amp:      158000.0 T:  18.0   Ms =   6.4
 OBN  BZ    dist:    2420.0   amp:       31652.9 T:   5.2   mB =   6.9
 OBN  BZ    dist:    2420.0   amp:        6234.6 T:   2.4   mb =   6.6
 OBN  BZ    dist:    2420.0   amp:      168000.0 T:  21.8   Ms =   6.4
 OBN  BZ    dist:    2420.0   amp:       49453.8 T:  19.6   MS =   6.4
 ARU  BZ    dist:    2954.0   amp:         269.7 T:   1.0   mb =   5.9
 ARU  BZ    dist:    2954.0   amp:       10130.1 T:   7.6   mB =   6.7
 ARU  BZ    dist:    2954.0   amp:       36322.6 T:  18.1   Ms =   6.0
 ARU  BZ    dist:    2954.0   amp:       16468.0 T:  16.1   MS =   6.1
 2012  524 2247 45.1 D  72.943   6.096  8.8F BER 20 1.8 6.3sBER 6.1SBER 6.4bBER
```

Output from location program: We use the same standard linearized inversion program (HYPOCENTER) to locate this event as used for the local event. The location is based on the IASP91 global travel-time model. The residuals are much larger than for the local event as the difference between the true regional model and IASP91 is significant. The largest residual here is more than 3 seconds. In the hypocenter determination we fixed the depth to 8.8 km and, using both P and S readings, we obtain a latitude of 72.943°N and longitude of 6.096°E. This compares to 73.055°N and 5.856°E for the preliminary location based on P arrivals only. The solution based on P and S is 15 km east of the USGS solution.

Based on all our amplitude and period measurements the following network average magnitude values were calculated:

Magnitude scale	Value
Mw (USGS)	6.2
mb (USGS)	5.7
mb	6.4
mB_BB	7.0
Ms_20	6.3
Ms_BB	6.1

Note that Ms_20 and Ms_BB are within 0.1 m.u. of the USGS Mw. In contrast, both our mb and mB_BB are significantly larger, with mb, based on only 4 measurements in the near teleseismic distance range between 2000 and 3000 km, even by 0.7 m.u. larger than USGS mb, based on 299 measurements at a much larger range of distances up to about 11,000 km. This may hint to larger calibration uncertainties of the Gutenberg-Richter (1956) Q function in the near teleseismic distance range, where wave propagation is largely influenced by the greater inhomogeneity of upper mantle wave propagation and attenuation. This may result in larger uncertainty of body-wave magnitude estimates, if they are available in only very limited number in the near teleseismic range. On the other hand, this earthquake has taken place on the North-Atlantic Ridge (see Google map below). Intra-oceanic ridge strike-slip earthquakes are often high stress drop events characterized by a much larger than average ratio of E_S/M_0 and thus much larger Me than Mw (e.g. Bormann and Di Giacomo, 2011; Choy, 2012, in IS 3.5). Then, mb and mB_BB may be much larger than usual too in their relation to long-period Mw and Ms. Therefore one might consider this as an alternative explanation, which is, however, neither supported by the much more representative USGS mb value (being rather normal for Mw = 6.2) nor by the relatively long and not very impulsive P waveforms. The latter are, in the case of high stress drop events, expected to be relatively short, impulse-like and of more high-frequency content (e.g., Fig. 3.6 in Chapter 3). Instead, the P-wave group is rather long for an Mw6.2 event, almost one minute, and relatively long-period.

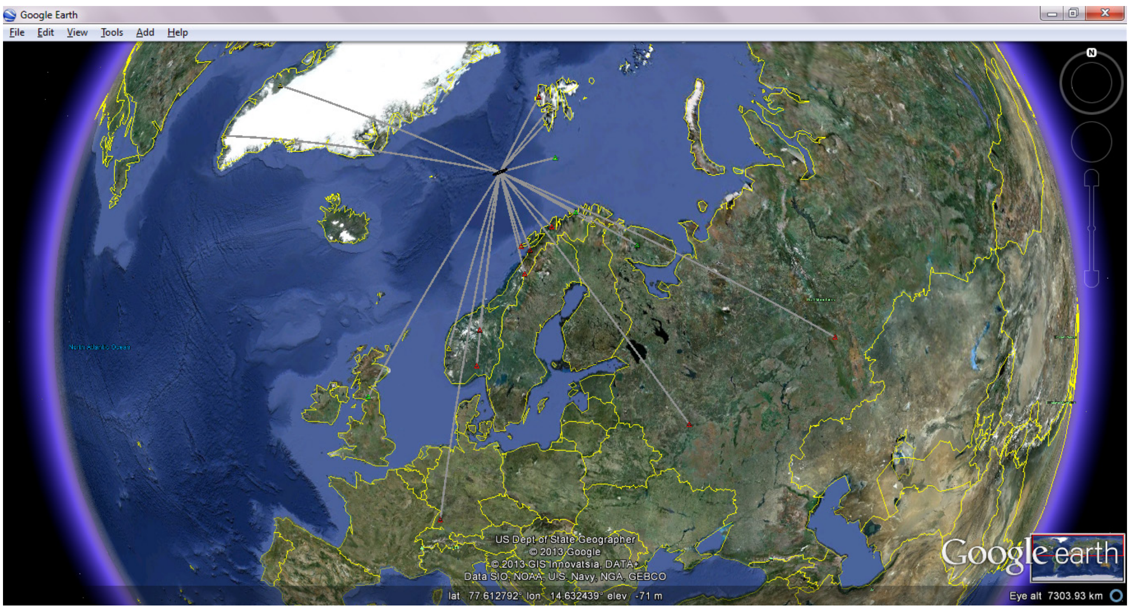

Location map in GoogleEarth: This map shows the location with its error ellipse on the Mid-Atlantic ridge and the stations that were used for the analysis and location.

4 Analysis of a shallow earthquake recorded at teleseismic distances (30° < Δ < 90°)

The earthquake chosen here as an example occurred in Russia at a shallow depth of 10 km (according to USGS). We extracted data from IRIS that was recorded on the Global Seismograph Network (GSN). All data used here were recorded on broadband stations.

The earthquake parameters provided by the USGS are:

Date:	14/02/2013
Origin time:	13:13:53.1 (UTC)
Latitude:	67.61°N
Longitude:	142.60°W
Depth:	10 km
Mw:	6.9

We now show the step-by-step procedure to analyze the earthquake.

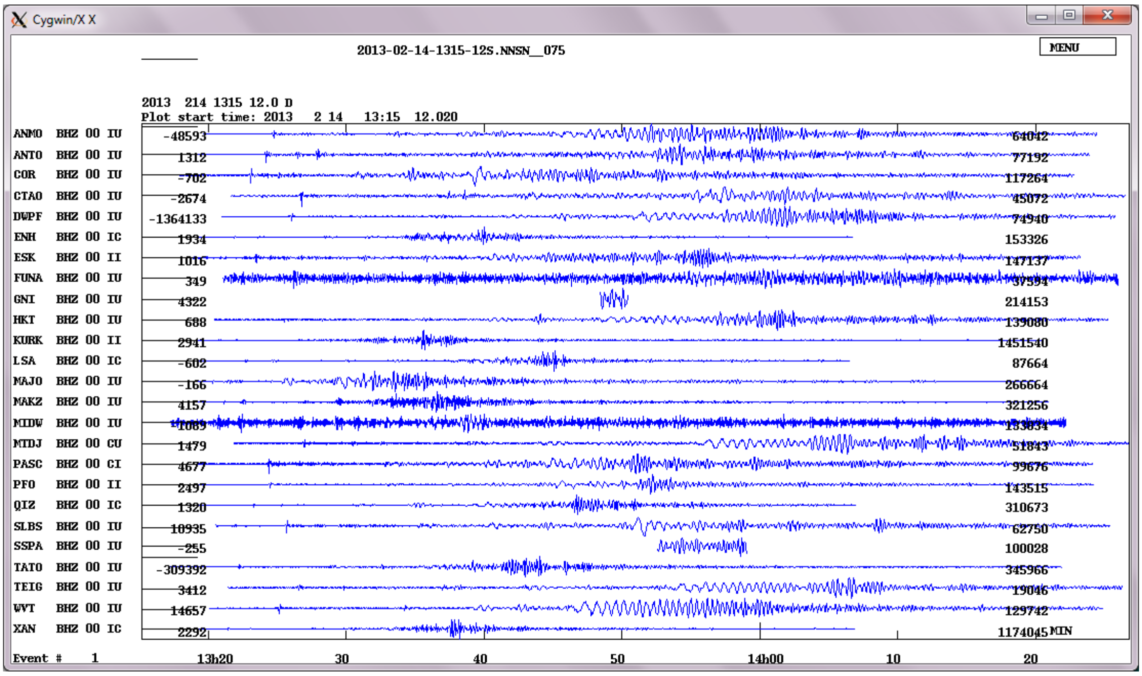

Multi-trace plot of vertical components, unfiltered: Record durations up to about 60 minutes at some stations and the observation of much larger surface-wave than body wave amplitudes hints to a large shallow earthquake at teleseismic distances.

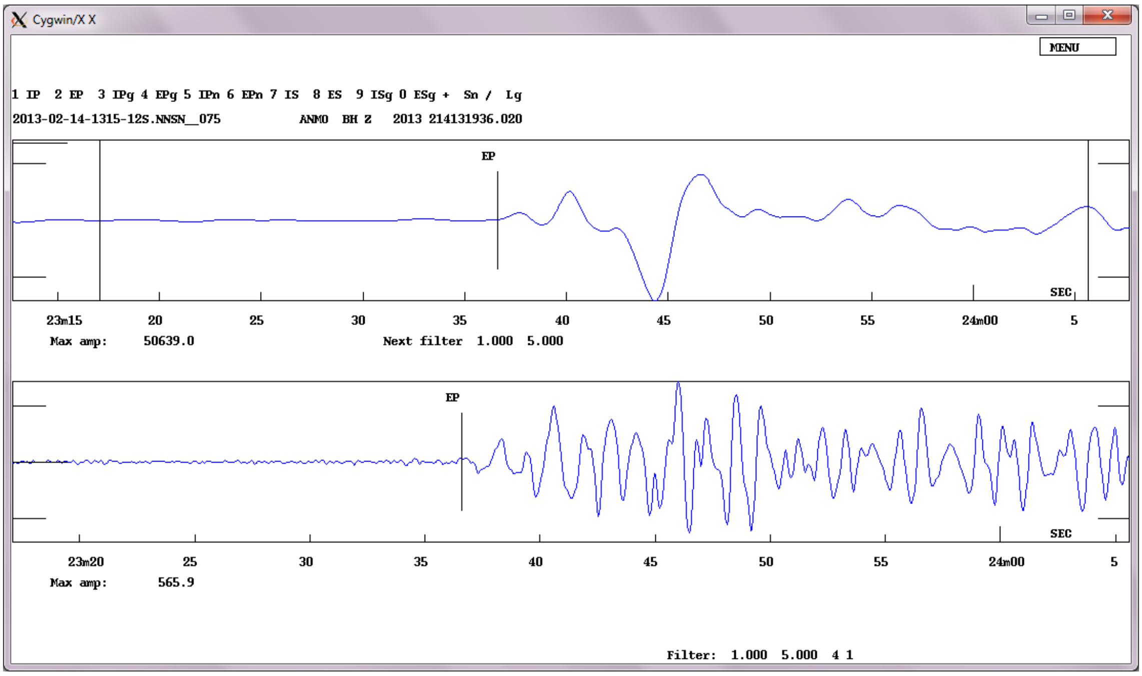

Vertical-component trace of station ANMO at Δ= 65.4°, unfiltered (top) and filtered 1-5 Hz (bottom): We start by reading the P arrivals that are very clear for this event. They can be read both on unfiltered (top) and high-pass filtered seismograms (bottom).

```
#    1 14 Feb 2013 13:15 12  D                                       ? 1

  date hrmn   sec      lat      long depth   no m    rms  damp erln erlt erdp
13 214 1313 51.82 6731.31N 142 49.6E   0.0   19 3   0.94 0.000 42.6 19.3236.1
 stn   dist   azm  ain w phas     calcphs hrmn tsec  t-obs  t-cal    res   wt di
 MAJO  3456 187.2 27.3 0 P        P       1320 10.0 378.22 379.99  -1.77 0.90*12
 KURK  3888 274.1 26.7 0 P        P       1320 45.3 413.45 413.76  -0.31 1.00* 9
 MAKZ  4098 267.2 26.3 0 P        P       1321  1.0 429.15 430.05  -0.90 0.97* 7
 XAN   4307 227.7 25.9 0 P        P       1321 18.1 446.28 446.03   0.25 1.00* 5
 ENH   4683 225.1 25.2 0 P        P       1321 45.2 473.41 474.06  -0.65 0.99* 5
 TATO  4945 208.1 24.6 0 P        P       1322  5.6 493.80 493.00   0.80 0.98* 7
 LSA   5384 245.7 23.7 0 P        P       1322 38.1 526.24 524.80   1.44 0.93* 3
 COR   5678  66.3 23.1 0 P        P       1322 57.4 545.60 544.19   1.41 0.94* 4
 QIZ   5863 220.3 22.7 0 P        P       1323  9.3 557.43 556.76   0.67 0.99* 5
 ESK   6093 337.0 22.2 0 P        P       1323 23.0 571.15 571.46  -0.31 1.00*11
 ANTO  6748 304.1 20.8 0 P        P       1324  5.6 613.77 613.41   0.36 1.00* 9
 PASC  6905  67.8 20.5 0 P        P       1324 14.8 622.99 623.05  -0.06 1.00* 4
 PFO   7029  66.6 20.3 0 P        P       1324 22.4 630.63 630.69  -0.06 1.00* 4
 ANMO  7271  57.6 19.7 0 P        P       1324 36.6 644.80 644.94  -0.14 1.00* 3
 WVT   7753  41.8 18.7 0 P        P       1325  2.0 670.19 672.03  -1.84 0.89* 2
 HKT   8152  50.7 17.9 0 P        P       1325 25.0 693.21 693.77  -0.56 0.99* 3
 SLBS  8298  65.2 17.6 0 P        P       1325 33.8 701.95 701.74   0.21 1.00* 3
 TEIG  9414  47.2 15.2 0 P        P       1326 27.4 755.63 756.06  -0.43 0.99* 2
 CTAO  9700 176.8 14.5 0 P        P       1326 39.3 767.43 768.26  -0.83 0.00  0
 MTDJ  9936  38.0 14.1 0 P        P       1326 52.7 780.87 778.91   1.96 0.88* 1

 2013  214 1313 51.8 D  67.522 142.826  0.0  TES 20 0.9
```

Output from the location program: Locating with the first P arrivals only, we obtain an epicenter location (67.522°N, 142.826°W) and depth = 0 km that is very close to the one given by the USGS. The depth is not constrained with the teleseismic P arrivals only.

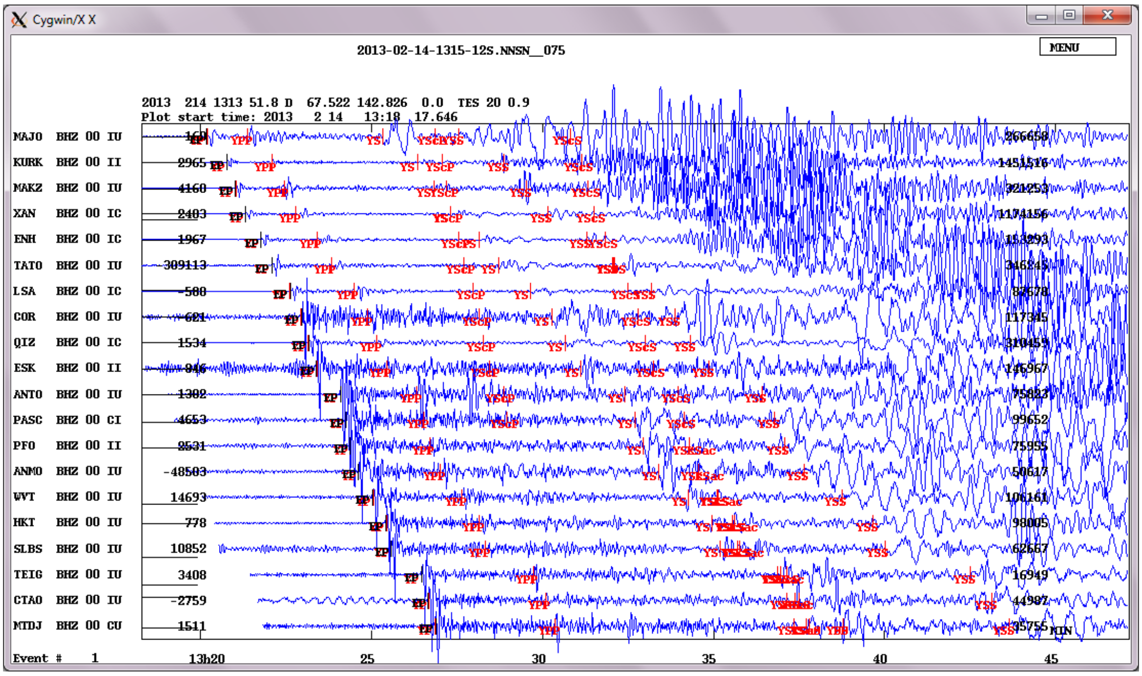

Multi-trace plot of vertical components, unfiltered: Plotted are the traces on which we have read the initial P. Based on the hypocenter obtained, we compute the synthetic arrival times of all phases. The traces are sorted by distance. The phases PP, S and SS are clear on all traces. We will now read the onset times of all these phases (plus P-wave first motion polarity), run the location program again with this additional information and see how the location changes.

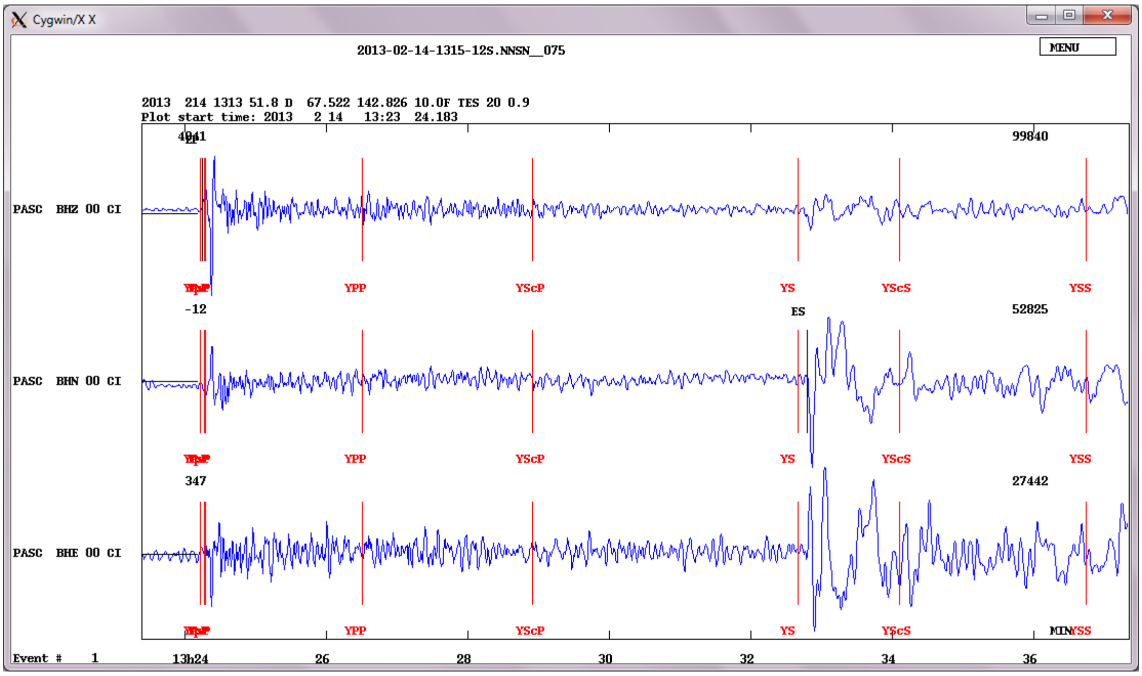

Three-component trace plot of station PASC at Δ=62.2°, unfiltered: For this station P on the vertical component and S on the N component are very clear. Other phases are not very clear. Note that we do not pick the onsets at the calculated arrival times (red bars) but only at the distinct onset of the real phases with large SNR (black bars).

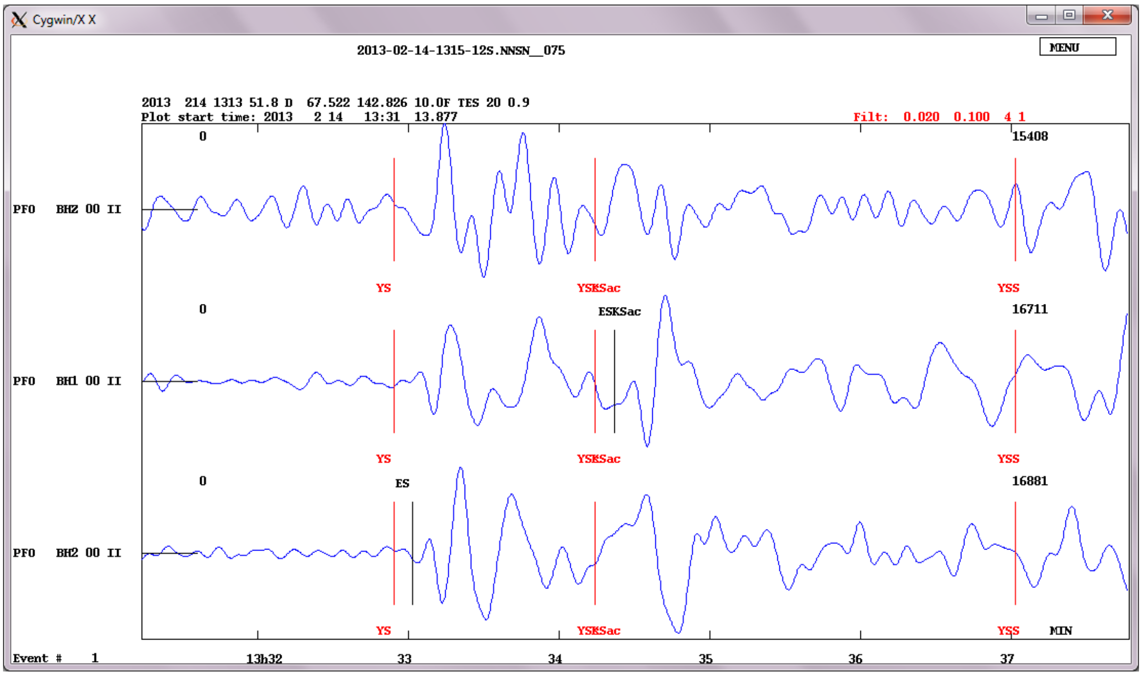

Three-component trace plot of station PFO at Δ= 63.3°, filtered 0.02-0.1 Hz: At this distance there is sufficient separation between S and SKSac to read both phases. The component codes of the horizontal components here are BH1 and BH2 to indicate that the instrument is not exactly aligned with the geographic directions. In this case, the direction of orientation is given with the component's metadata and can be used to rotate into a NS-EW system.

```
#    1 14 Feb 2013 13:13 51  D  67.522 142.826         0.9     TES   20  ? 1

  date hrmn   sec      lat      long depth   no m    rms  damp erln erlt erdp
13 214 1313 54.89 6748.67N 142 10.4E   0.1   55 3   5.94 0.000 92.7 44.2 39.3
 stn   dist   azm  ain w phas    calcphs hrmn tsec  t-obs  t-cal    res   wt di
 MAJO  3485 186.1 42.8 0 PP      PnPn    1321 22.8 447.91 445.00   2.91 1.00  4
 MAJO  3485 186.1 27.3 0 P       P       1320 10.0 375.15 382.25  -7.11 1.00  2
 MAJO  3485 186.1 28.1 0 S       S       1325 19.8 684.86 691.48  -6.62 1.00  6
 KURK  3858 273.1 26.8 0 P       P       1320 45.3 410.38 411.44  -1.06 1.00  1
 KURK  3858 273.1 40.6 0 PP      PnPn    1322  2.6 487.69 487.73  -0.04 1.00  3
 KURK  3858 273.1 27.7 0 S       S       1326 18.9 744.06 743.37   0.69 1.00  4
 MAKZ  4072 266.2 26.4 0 P       P       1321  1.0 426.08 428.05  -1.98 1.00  1
 MAKZ  4072 266.2 39.7 0 PP      PnPn    1322 27.4 512.54 511.60   0.94 1.00  2
 MAKZ  4072 266.2 46.9 0 SS      SnSn    1329 16.4 921.49 924.72  -3.23 1.00  9
 XAN   4308 226.6 25.9 0 P       P       1321 18.1 443.21 446.13  -2.92 1.00  0
 XAN   4308 226.6 34.8 0 PP      PP      1322 52.7 537.78 535.32   2.46 1.00  1
 XAN   4308 226.6 27.1 0 S       S       1327 16.3 801.38 805.45  -4.08 1.00  2
 ENH   4687 224.0 25.2 0 P       P       1321 45.2 470.34 474.30  -3.96 1.00  0
 ENH   4687 224.0 34.3 0 PP      PP      1323 30.7 575.79 572.36   3.43 1.00  1
 ENH   4687 224.0 26.5 0 S       S       1328  6.2 851.27 856.26  -4.99 1.00  2
 ENH   4687 224.0 36.7 0 SS      SS      1331 20.01045.071046.08  -1.01 1.00  3
 TATO  4960 207.1 24.6 0 P       P       1322  5.6 490.73 494.12  -3.39 1.00  1
 TATO  4960 207.1 33.8 0 PP      PP      1323 57.4 602.48 598.76   3.72 1.00  2
 TATO  4960 207.1 26.0 0 S       S       1328 43.4 888.52 892.20  -3.68 1.00  3
 LSA   5373 244.7 23.7 0 P       P       1322 38.1 523.17 523.96  -0.80 1.00  0
 LSA   5373 244.7 28.4 0 PP      PP      1324 35.9 641.06 636.87   4.19 1.00  1
 LSA   5373 244.7 25.3 0 S       S       1329 40.4 945.49 946.59  -1.10 1.00  1
 LSA   5373 244.7 29.2 0 SS      SS      1333 24.01169.111158.32  10.78 1.00  2
 COR   5690  66.0 23.1 0 P       P       1322 57.4 542.53 545.00  -2.47 1.00  1
 COR   5690  66.0 24.7 0 S       S       1330 21.9 986.97 985.30   1.67 1.00  2
 COR   5690  66.0 28.6 0 SS      SS      1334 25.71230.761203.01  27.74 1.00  3
 QIZ   5870 219.4 22.7 0 P       P       1323  9.3 554.36 557.21  -2.85 1.00  0
 QIZ   5870 219.4 28.1 0 PP      PP      1325 15.6 680.66 677.02   3.64 1.00  1
 QIZ   5870 219.4 24.4 0 S       S       1330 41.41006.491007.80  -1.32 1.00  2
 QIZ   5870 219.4 28.5 0 SS      SS      1334 45.31250.381228.62  21.76 1.00  2
 ESK   6053 336.5 22.3 0 P       P       1323 23.0 568.08 568.79  -0.71 1.00  2
 ANTO  6707 303.4 20.9 0 P       P       1324  5.6 610.70 610.87  -0.17 1.00  2
 ANTO  6707 303.4 27.5 0 PP      PP      1326 22.1 747.22 744.41   2.81 1.00  3
 ANTO  6707 303.4      0                 1327 47.7  832.8
 ANTO  6707 303.4 22.8 0 S       S       1332 27.01112.141107.57   4.57 1.00  6
 PASC  6918  67.4 20.5 0 P       P       1324 14.8 619.92 623.83  -3.91 1.00  1
 PASC  6918  67.4 22.4 0 S       S       1332 47.81132.861131.89   0.97 1.00  2
 PFO   7042  66.2 20.2 0 P       P       1324 22.4 627.56 631.41  -3.85 1.00  1
 PFO   7042  66.2 22.2 0 S       S       1333  1.51146.591146.11   0.48 1.00  2
 PFO   7042  66.2 13.3 0 SKSac   SKSac   1334 22.11227.241226.38   0.86 1.00  1
 ANMO  7276  57.2 19.7 0 P       P       1324 36.6 641.73 645.27  -3.54 1.00  1
 ANMO  7276  57.2 21.7 0 S       S       1333 24.01169.091172.25  -3.16 1.00  2
 WVT   7747  41.4 18.8 0 P       P       1325  2.0 667.12 671.69  -4.57 1.00  1
 WVT   7747  41.4 20.8 0 S       S       1334 11.71216.831222.45  -5.62 1.00  2
 WVT   7747  41.4 27.7 0 SS      SS      1338 42.61487.751492.76  -5.01 1.00  3
 HKT   8153  50.2 17.9 0 P       P       1325 25.0 690.14 693.79  -3.65 1.00  1
 HKT   8153  50.2 20.0 0 S       S       1334 55.21260.271264.73  -4.46 1.00  2
 SLBS  8309  64.7 17.6 0 P       P       1325 33.8 698.88 702.32  -3.44 1.00  1
 SLBS  8309  64.7 19.7 0 S       S       1335 15.71280.781281.06  -0.29 1.00  2
 SLBS  8309  64.7 27.3 0 SS      SS      1340 12.21577.301570.17   7.13 1.00  3
 TEIG  9412  46.6 15.2 0 P       P       1326 27.4 752.56 755.95  -3.39 1.00  0
 TEIG  9412  46.6 25.1 0 PP      PP      1329 48.6 953.66 952.02   1.64 1.00  1
 CTAO  9733 176.2 14.4 0 P       P       1326 39.3 764.36 769.71  -5.35 0.00  0
 CTAO  9733 176.2 24.8 0 PP      PP      1330  6.6 971.71 975.50  -3.79 1.00  2
 MTDJ  9927  37.4 10.3 0 SKSac   SKSac   1337 24.11409.231409.91  -0.68 1.00  1
 MTDJ  9927  37.4 24.6 0 PP      PP      1330 25.7 990.79 989.60   1.18 1.00  1
 MTDJ  9927  37.4 14.1 0 P       P       1326 52.7 777.80 778.52  -0.72 1.00  0

 2013  214 1313 54.9 D  67.811 142.173  0.1  TES 20 5.9
```

Output from the location program: Using additional phases the location changes slightly, but without readings of depth phases or P-wave onsets very near to this shallow source the depth cannot be better resolved compared to the USGS.

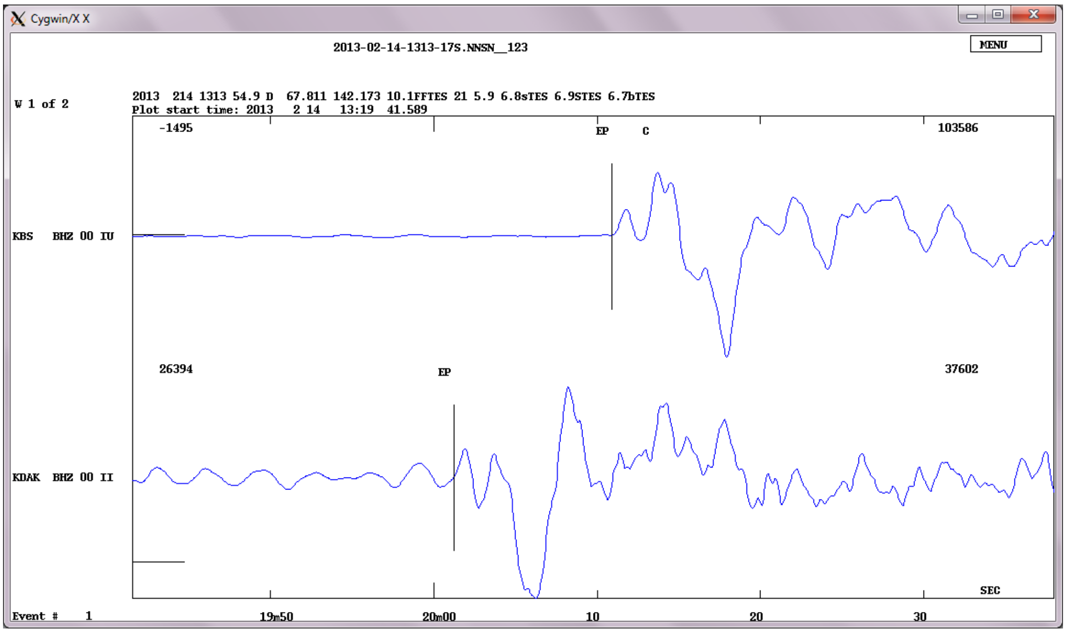

Vertical component traces of stations KBS and KDAK, unfiltered: We try to read first-motion P-wave polarities (upward motion = C = + = compressional, downward motion = D = – = dilatational) which can allow us to estimate a fault-plane solution for this earthquake. For station KBS (top) it is possible to read the polarity, which is upward (compression). For station KDAK it is not possible to read the polarity, although we were tempted to read this as a downward motion (dilatation). As seen further down, the selected data set does not have stations that are for sure in a dilatational quadrant, however, the position of all our compressional readings (see next figure) are in agreement with Global CMT fault-plane solution.

The following solution was provided by the Global CMT catalog (www.globalcmt.org) for this event. The solution shows an oblique thrust mechanism:

201302141313A EASTERN SIBERIA, RUSSIA

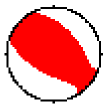

```
Date: 2013/ 2/14   Centroid Time: 13:13:58.6 GMT
Lat=  67.71  Lon= 142.62
Depth= 12.0   Half duration= 5.2
Centroid time minus hypocenter time:  5.5
Moment Tensor: Expo=26  1.030 -0.627 -0.404 0.335 0.075 0.729
Mw = 6.7     mb = 0.0     Ms = 6.6    Scalar Moment = 1.2e+26
Fault plane:  strike=327    dip=42   slip=115
Fault plane:  strike=115    dip=52   slip=69
```

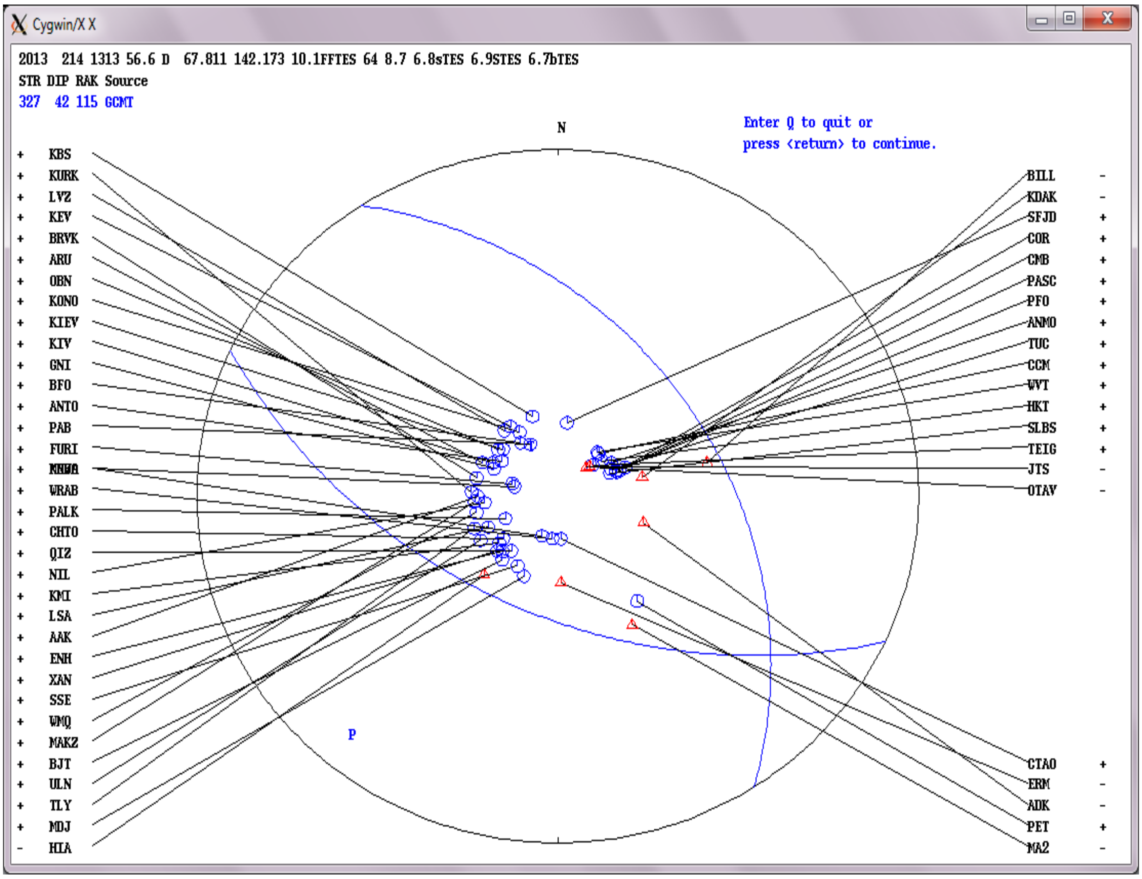

Fault-plane solution plot: This plot is created in SEISAN and shows the solution given by the Global CMT catalog together with polarities read from the example. We can see that all our observations lie near the center of the focal sphere and are likely compressions. However, the readings we made show compression and dilatation, and most likely the dilatational readings are wrong. Although looking at more than 100 stations from the global networks, we do not have good enough coverage of the focal sphere as all our rays to teleseismic stations only leave the source downward near the vertical. In contrast, the moment tensor solution (based on full waveforms from P, S and surface waves) normally requires only few stations to obtain a good solution. Using complementary to first-motion polarity readings in SEISAN also S/P amplitude ratios for better constraining fault-plane solutions is possible for local and teleseismic earthquakes. While the use of amplitude ratios did not help with this example, Figure 7.26 in Havskov and Ottemöller (2010) gives an example of teleseismic fault plane solution using amplitude ratios. The polarity readings made by us on individual station records (open circles = C, triangles = D) are given on the side with a link to the azimuth and angle of incidence of the corresponding phase projected onto the focal sphere.

Finally, we demonstrate the magnitude determinations for this earthquake:

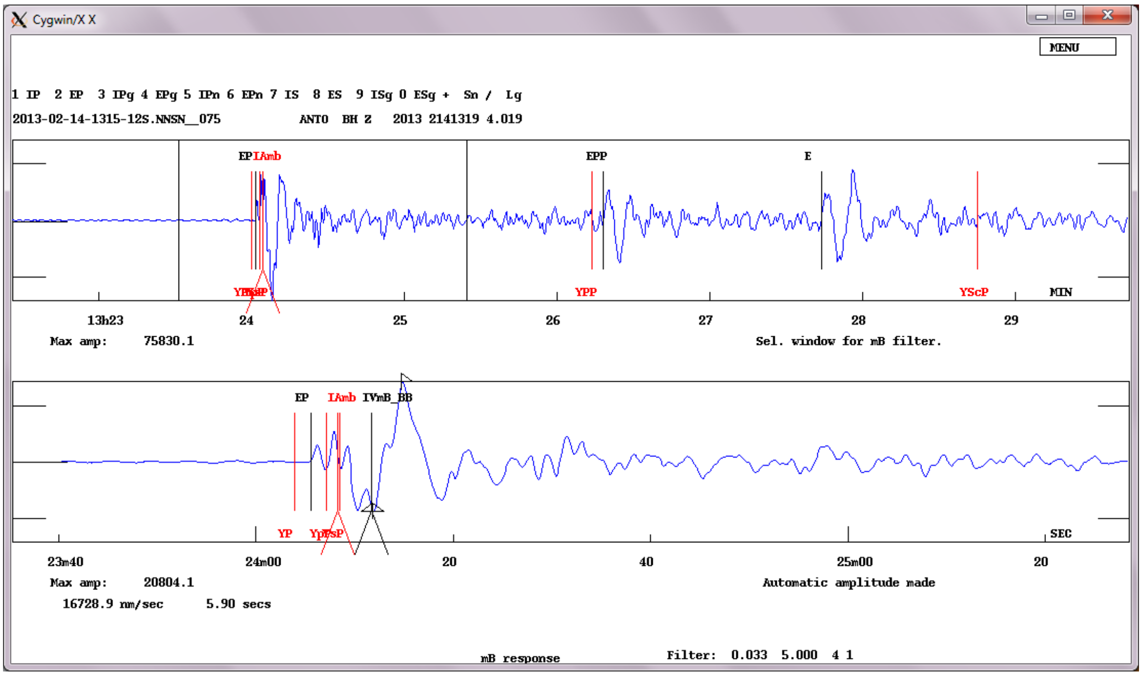

Traces of station ANTO at Δ= 60.3°, mB_BB filter: First we read amplitudes for mb and mB_BB. Measured are the largest P-wave amplitude prior to PP, depth phases of P included, on the vertical component of simulated short-period WWSSN, respectively velocity broadband records. The position of the earlier Iamb measurement has been plotted here on the mB_BB filtered trace only for comparison by a red arrow-bar. Details of teleseismic body-wave magnitudes are given in the regional event example in section 3 above and in IS 3.3.

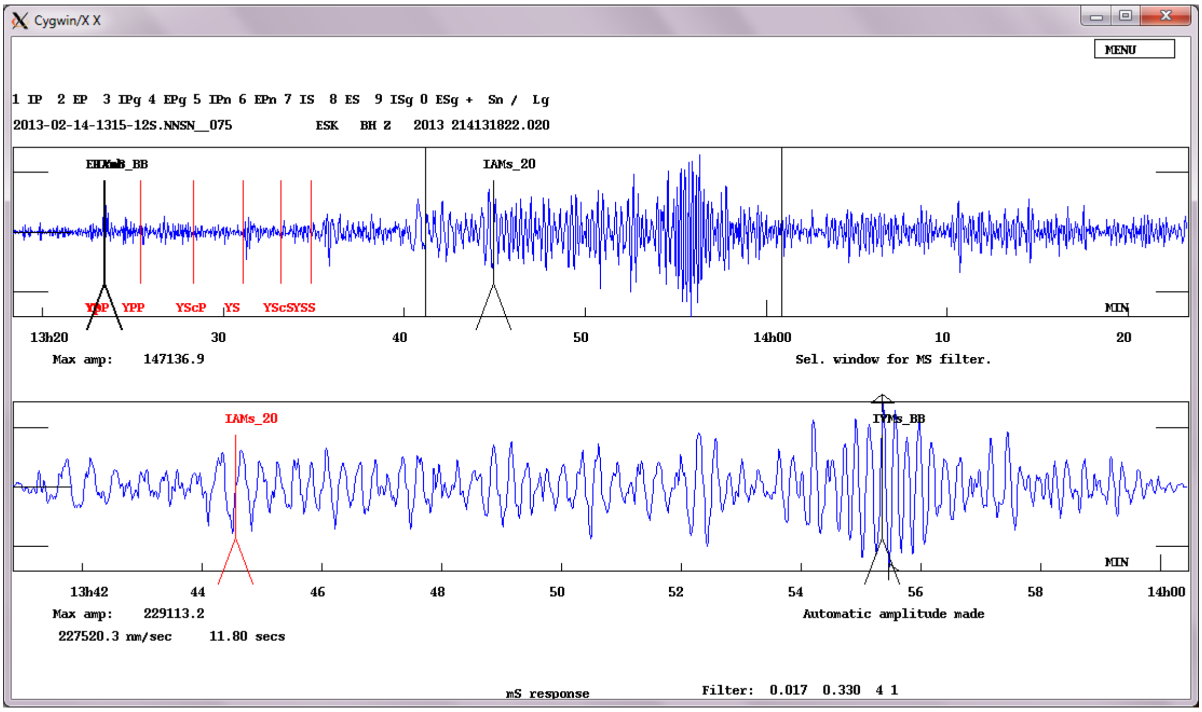

Traces of station ESK at Δ= 54.4°, Ms_BB filter: Next we determine the two IASPEI standard surface-wave magnitudes. The bottom trace shows the reading position of the Ms_BB amplitude IVMs_BB (black arrow-bar) on an instrument corrected broadband velocity trace.

The top trace is unfiltered and shows the time selection for the bottom trace. Note that the IAMs_20 amplitude has already been read on another, WWSSN-LP filtered, record, before. However, the position of its measurement is shown here too for comparison (marked by a red arrow-bar). While the largest Ms_20 displacement amplitude has a period of 21 s, the period of the 10.5 min later arriving largest Ms_BB velocity amplitude is 11.80 s only. For more details on the determination of teleseismic surface-wave magnitude see the regional event example in section 3 as well as IS 3.3.

Computing the average magnitudes from all amplitude observations we get the values below:

Magnitude scale	**Value**
Mw (USGS)	6.9
mb	6.7
mB_BB	7.3
Ms_20	6.9
Ms_BB	6.9

In this case the surface wave magnitudes Ms_20 and Ms_BB agree perfectly with Mw(USGS) and are equal amongst each other although Ms_BB has been measured at a much shorter period and a later time than Ms_20. mB_BB is significantly larger than mb, and somewhat larger than the two Ms and the Mw magnitude, as expected for earthquakes of Mw = 6.9 according to Utsu (2002) and Fig. 3.70 in section 3.2.9.1 of the forthcoming revised Chapter 3).

The amplitudes and periods that were read for computing the magnitudes are summarized in the following table. Note that here the abridged internal magnitude nomenclature used in SEISAN stands for: mb = mb, mB = mB_BB, Ms = Ms_20 and MS = Ms_BB.

XAN	BZ	dist:	4308.0	amp:	1498.7	T:	1.8	mb =	6.3
XAN	BZ	dist:	4308.0	amp:	22757.5	T:	8.8	mB =	7.0
ENH	BZ	dist:	4687.0	amp:	959.5	T:	1.5	mb =	6.3
ENH	BZ	dist:	4687.0	amp:	17567.1	T:	8.8	mB =	6.9
ENH	BZ	dist:	4687.0	amp:	120000.0	T:	10.9	MS =	7.3
ENH	BZ	dist:	4687.0	amp:	184000.0	T:	18.6	Ms =	7.0
TATO	BZ	dist:	4960.0	amp:	436.4	T:	0.9	mb =	6.3
TATO	BZ	dist:	4960.0	amp:	20681.6	T:	9.0	mB =	7.2
TATO	BZ	dist:	4960.0	amp:	111000.0	T:	18.9	Ms =	6.8
TATO	BZ	dist:	4960.0	amp:	81389.9	T:	11.8	MS =	7.2
COR	BZ	dist:	5690.0	amp:	18587.7	T:	3.8	mB =	7.2
COR	BZ	dist:	5690.0	amp:	778.2	T:	1.1	mb =	6.5
COR	BZ	dist:	5690.0	amp:	11899.5	T:	15.7	MS =	6.4
COR	BZ	dist:	5690.0	amp:	31700.7	T:	18.9	Ms =	6.4
ESK	BZ	dist:	6053.0	amp:	6275.4	T:	1.1	mb =	7.6
ESK	BZ	dist:	6053.0	amp:	171000.0	T:	8.5	mB =	8.2
ESK	BZ	dist:	6053.0	amp:	336000.0	T:	20.8	Ms =	7.4
ESK	BZ	dist:	6053.0	amp:	228000.0	T:	11.8	MS =	7.7
ANTO	BZ	dist:	6707.0	amp:	721.5	T:	1.2	mb =	6.7
ANTO	BZ	dist:	6707.0	amp:	16728.9	T:	5.9	mB =	7.3
ANTO	BZ	dist:	6707.0	amp:	57305.5	T:	19.2	Ms =	6.7
ANTO	BZ	dist:	6707.0	amp:	20010.4	T:	20.0	MS =	6.8
ANMO	BZ	dist:	7276.0	amp:	9820.2	T:	3.8	mB =	7.2
ANMO	BZ	dist:	7276.0	amp:	892.4	T:	2.0	mb =	6.6
ANMO	BZ	dist:	7276.0	amp:	18195.2	T:	21.0	MS =	6.8
ANMO	BZ	dist:	7276.0	amp:	59228.9	T:	21.3	Ms =	6.8
WVT	BZ	dist:	7747.0	amp:	68435.1	T:	20.2	Ms =	6.9
WVT	BZ	dist:	7747.0	amp:	20200.8	T:	19.0	MS =	6.9
DWPF	BZ	dist:	8770.0	amp:	1956.5	T:	2.2	mb =	6.8
DWPF	BZ	dist:	8770.0	amp:	11188.1	T:	3.6	mB =	7.1
DWPF	BZ	dist:	8770.0	amp:	74362.7	T:	22.0	Ms =	7.0
DWPF	BZ	dist:	8770.0	amp:	22267.2	T:	23.6	MS =	7.0
TEIG	BZ	dist:	9412.0	amp:	12224.9	T:	2.9	mB =	7.3
TEIG	BZ	dist:	9412.0	amp:	853.1	T:	1.4	mb =	6.8
TEIG	BZ	dist:	9412.0	amp:	18134.1	T:	21.4	MS =	7.0
TEIG	BZ	dist:	9412.0	amp:	58385.9	T:	20.6	Ms =	7.0
CTAO	BZ	dist:	9733.0	amp:	686.2	T:	2.0	mb =	6.6
CTAO	BZ	dist:	9733.0	amp:	4437.9	T:	19.5	MS =	6.4
CTAO	BZ	dist:	9733.0	amp:	13972.4	T:	21.4	Ms =	6.3

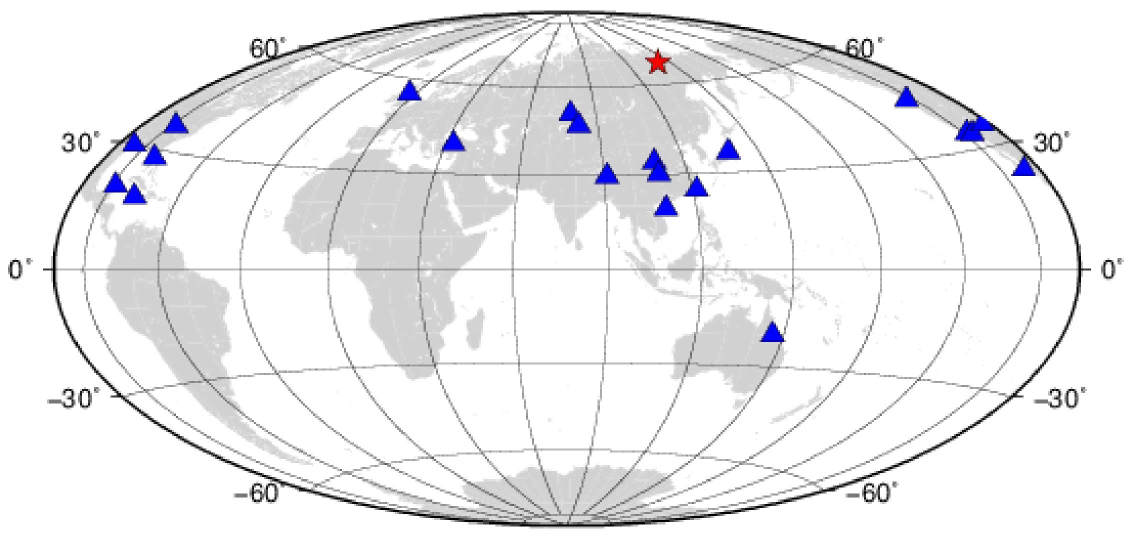

Map showing the epicenter (red star) and stations (blue triangles) used here.

5 Analysis of an intermediate depth earthquake at teleseismic distances

The earthquake chosen here as example occurred in Colombia at an intermediate depth of 129 km (depth by USGS). We extracted data from IRIS that were recorded by the Global Seismograph Network (GSN). All data used here were recorded on broadband stations.

The earthquake parameters provided by the USGS are:

Date:	09/02/2013
Origin time:	14:16:06.3 (UTC)
Latitude:	1.14°N
Longitude:	77.36°W
Depth:	129 km
Mw:	7.0

We now show the step-by-step procedure to analyze the earthquake.

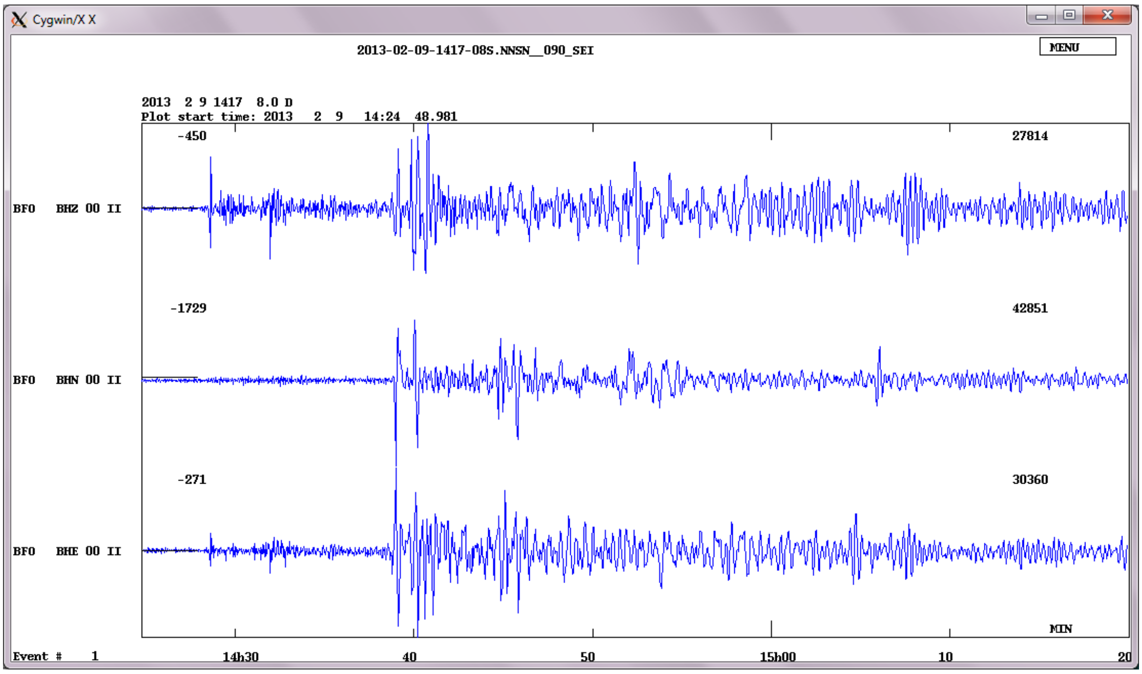

Three-component trace plot of station BFO at Δ= 86.4°, unfiltered: Looking at one of the stations, we can see that we are dealing with an earthquake at teleseismic distance as the record shown extends to almost one hour. The seismograms show very clear body-wave phase arrivals, which we will try to identify. The lack of more long-period and dispersed surface waves, however, points at a deep hypocenter. We will start to pick first P arrivals to get an initial estimate of the location, then we try to identify depth phases and other later phases for improved hypocenter determination and finally we use the 3-component record of station BFO only for a single-station event location.

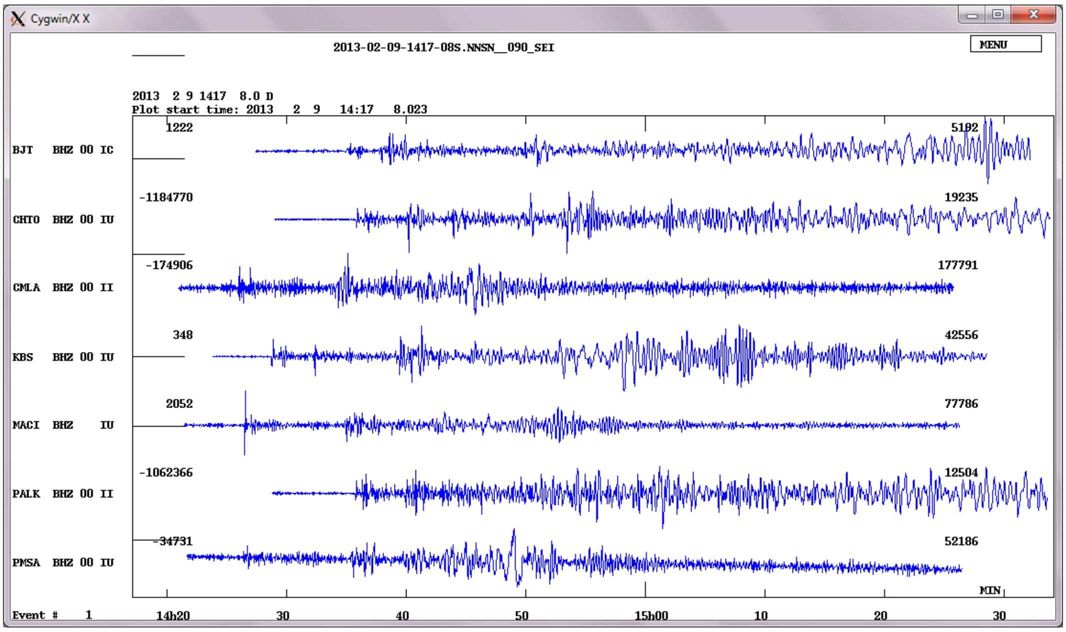

Multi-trace plot of vertical components, unfiltered: Shown is only a selection of the stations that are part of the sample data set for this event.

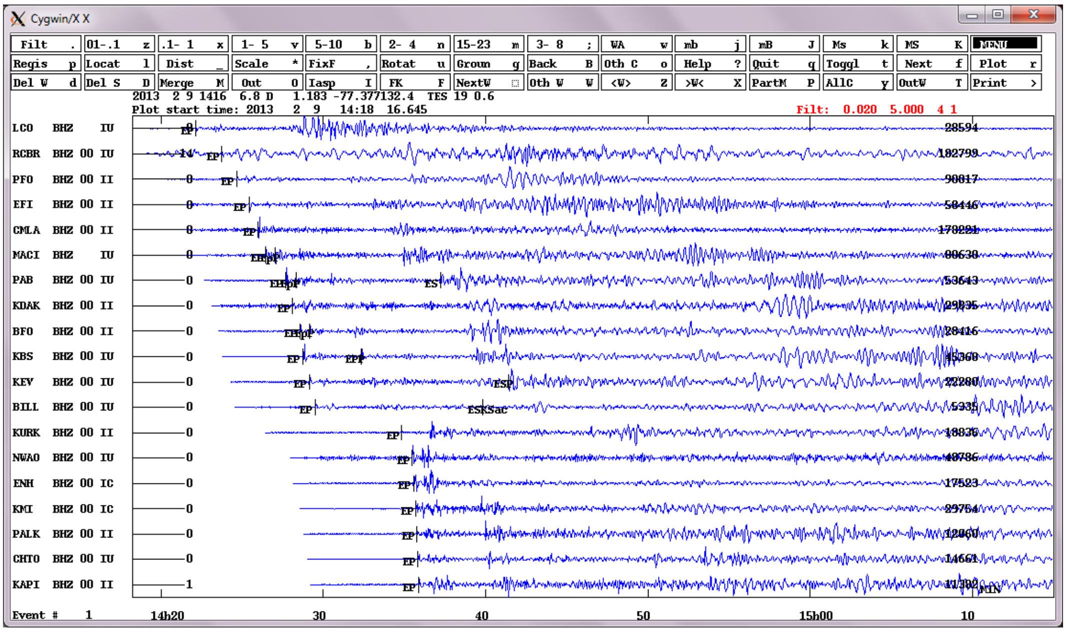

Vertical-component traces for which phases are picked, filtered 0.02-5 Hz: These traces are sorted by epicentral distance, ranging from 30.7° to 162.7°. Beside the P first arrival, at some of the traces also clear later arrivals have been marked and identified. Note that from station KURK downward the strong delay of the first arriving longitudinal waves is due to the Earth core shadow for direct P waves. In fact, the group of later arrivals, annotated here as P, relate to different branches of PKP core phases and likely also their depth phases. Also note several distinct onsets following within the first minute after the P onset and well before the arrival of PP. For a first event location we will only use the P and PKP first arrivals. Later, we will zoom into the first few minutes of records in order to find depth phases of P and PKP.

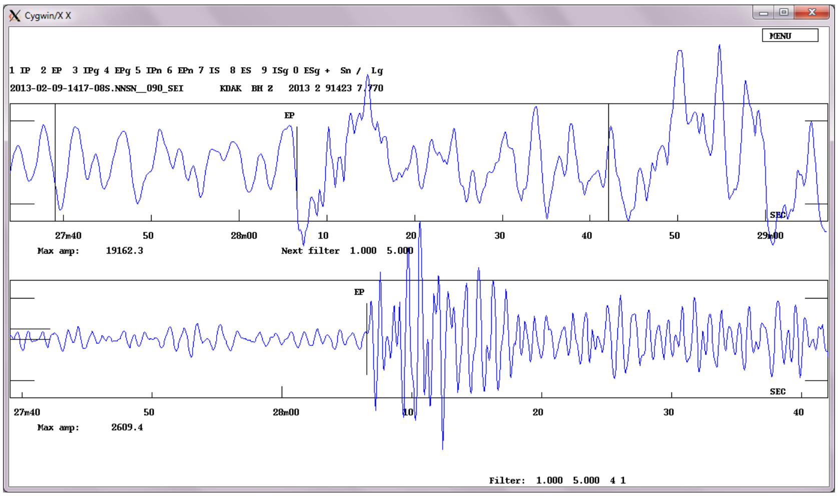

Vertical-component trace of station KDAK at Δ=81.2°, top unfiltered, bottom filtered 1-5 Hz: Whereas most of the P arrivals in the earlier shown record section of all stations had a good SNR, this is an example where the P arrival can only be picked after filtering the trace. The time window of the expanded lower trace is marked by the vertical lines on the unfiltered top trace. The use of the filter introduces a small phase shift and at some observatories it is common practice to read all stations with the same filter. However, as long as the phase shift is small as compared to the reading error one can, depending on the signal-to-noise ratio (SNR) of individual stations, chose the best filter or no filter. There may also be stations where the SNR is too low and phases will not be read. This is better than reading false phases.

```
#    1  9 Feb 2013 14:17  8  D                                    ? 1

  date hrmn   sec      lat      long depth   no m    rms  damp erln erlt erdp
13 2 9 1416  6.75  110.98N  77 22.6W 132.4   19 3   0.64 0.000 15.6 12.3 48.7
 stn   dist   azm  ain w phas     calcphs hrmn tsec  t-obs  t-cal    res   wt di
 LCO   3417 168.5 39.7 0 P        P       1422  9.6 362.83 362.82   0.01 1.00*17
 RCBR  4675 100.0 36.2 0 P        P       1423 45.0 458.23 458.28  -0.05 1.00*11
 PFO   5430 315.6 33.7 0 P        P       1424 39.4 512.70 511.80   0.90 0.97*21
 EFI   6139 165.5 31.5 0 P        P       1425 25.1 558.33 558.79  -0.47 0.99* 9
 CMLA  6665  46.1 29.8 0 P        P       1425 59.0 592.23 591.93   0.30 1.00* 6
 MACI  7120  59.1 28.4 0 P        P       1426 27.2 620.43 619.48   0.95 0.97* 5
 PAB   8482  49.6 24.3 0 P        P       1427 40.6 693.81 694.00  -0.20 1.00* 3
 KDAK  9032 328.4 22.6 0 P        P       1428  6.6 719.81 720.90  -1.09 0.96* 5
 BFO   9603  41.8 20.8 0 P        P       1428 32.9 746.20 747.04  -0.84 0.98* 2
 KBS   9876  11.1 19.9 0 P        P       1428 45.8 759.07 758.66   0.41 0.99* 1
 KEV  10448  19.8 19.4 0 P        P       1429  8.0 781.28 782.45  -1.18 0.96* 1
 BILL 10966 340.1 18.8 0 P        Pdif    1429 29.2 802.41 803.17  -0.76 0.98* 2
 KURK 13847  18.3  8.0 0 P        PKPdf   1434 49.31122.541123.03  -0.49 0.99* 2
 NWAO 16204 202.0  7.0 0 P        PKPdf   1435 28.61161.821161.84  -0.02 1.00* 4
 ENH  16480 348.7  6.8 0 P        PKPdf   1435 33.21166.431165.98   0.45 0.99* 2
 KMI  17127 359.8  5.9 0 P        PKPdf   1435 42.81176.031175.09   0.94 0.97* 2
 PALK 17430  68.7  5.4 0 P        PKPdf   1435 45.81179.101178.53   0.57 0.99* 3
 CHTO 17789  10.1  4.8 0 P        PKPdf   1435 49.51182.781182.46   0.32 1.00* 2
 KAPI 18088 257.1  4.2 0 P        PKPdf   1435 52.21185.461185.29   0.16 1.00* 3

 2013  2 9 1416  6.8 D   1.183 -77.377132.4  TES 19 0.6
```

Output from the location program on the previous page: Locating with the first P arrivals only, we obtain a hypocenter location (1.183°N, 77.377°W and depth = 132.4 km) that is very close to the one given by the USGS. The depth estimate is perhaps better than expected in this case without the use of depth phases. However, we will now try to use the depth phases we noticed on a number of seismograms. We have so far read all first arrivals as P. The location program determines which phase arrives first. In our example we have P (until station KEV), Pdif (station BILL) and PKPdf (from station KURK onward).

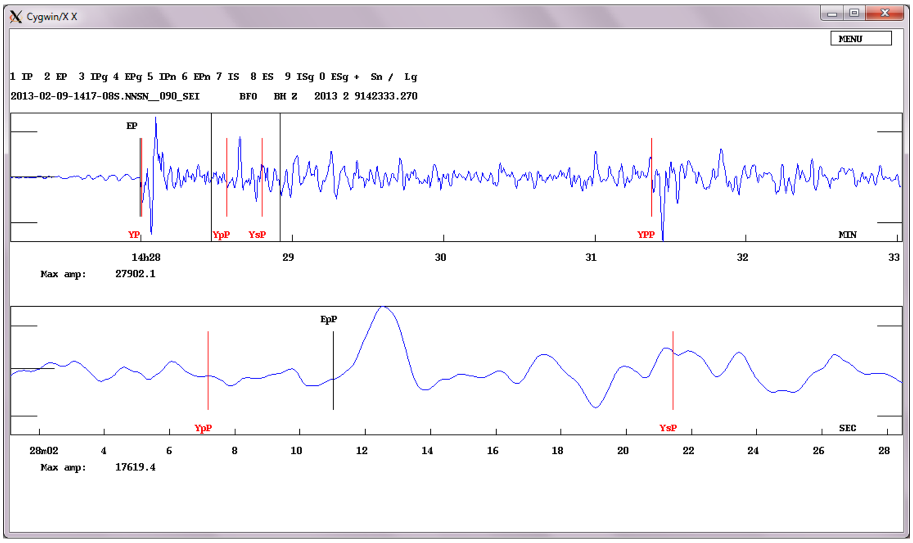

Vertical-component trace for station BFO at Δ= 86.4°, unfiltered: For this station we have computed synthetic arrival times based on our initial location, which are marked with red bars. We can see distinct phases arriving near the computed pP, sP and PP times. The bottom trace shows the picking of pP about 4 s after the predicted arrival, but there is no clear new energy arrival around the expected sP onset. Note, however, that sP may sometimes be even a stronger phase than pP. The amplitude relationship between these two depth phases depends on the radiation pattern of the source mechanism, which is different for P and S waves (see Chapter 3, section 3.4.1, Figs. 3.100-104), and on the different take-off angles of pP and sP from the source (see Chapter 2, section 2.6.3 with figures). From the measured travel-time difference of 38.2 s between pP and P we estimate a source depth of about 150 km, some 20 km deeper than the source depth calculated by the USGS.

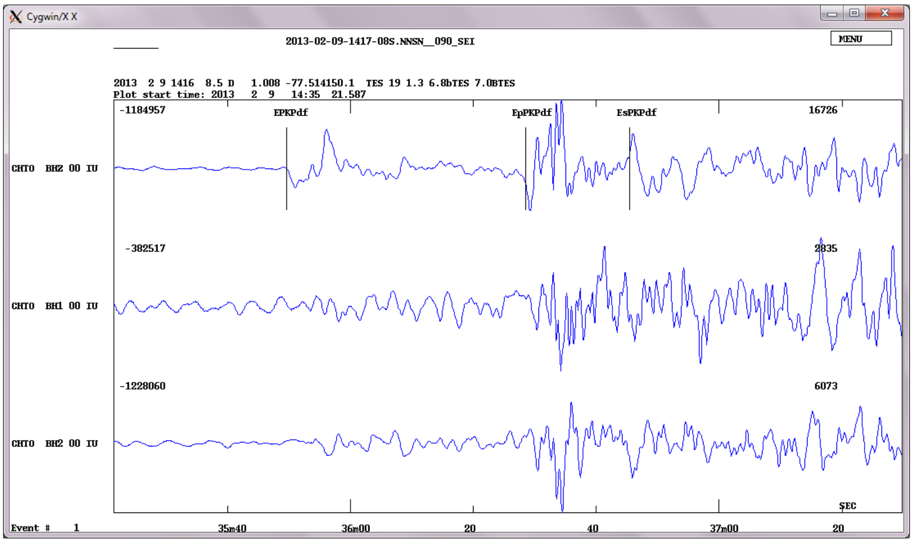

Three-component trace of station CHTO at Δ=160.0°, unfiltered: Knowing from the first location of the earthquake that the station is 160° away the first arrival at 35m50s is clearly not P, as originally marked, but PKPdf. The larger onset about 5 s later is a second phase of the same event, yet the much stronger sharp wave onset at about 36m28s is obviously the depth phase pPKPdf and the onset at about 36m45s the depth phase sPKPdf. Note that the travel-time difference pPKPdf-PKPdf of 38 s perfectly agrees with the time difference pP-P = 38.2 s measured at station BFO. Note that the differential times such as pP-P and sP-P should be near constant over a distance range.

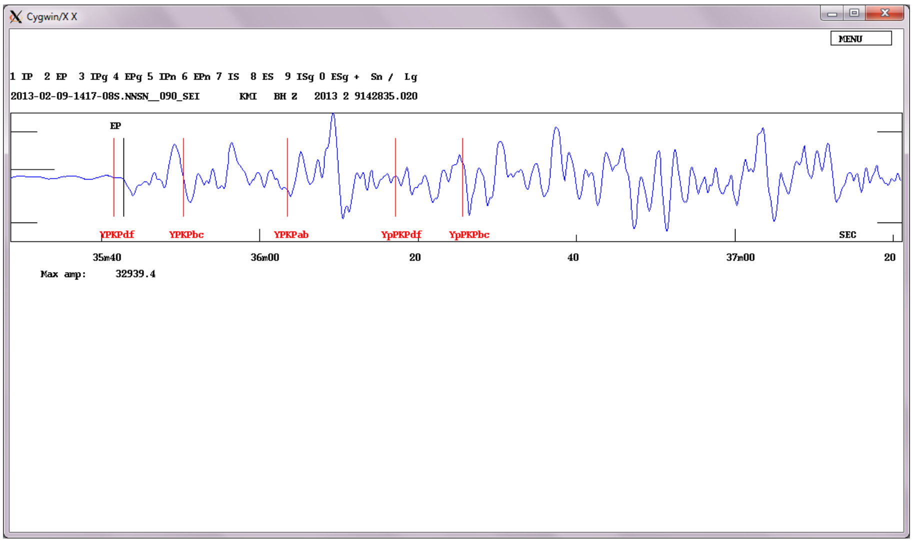

Vertical-component trace for station KMI at Δ=154.0°, unfiltered: In this example we can see onsets that relate to the different travel-time branches of PKP. The corresponding depth phase times are also shown and phases are visible. Core phases are often most clear in the frequency band 1-5 Hz.

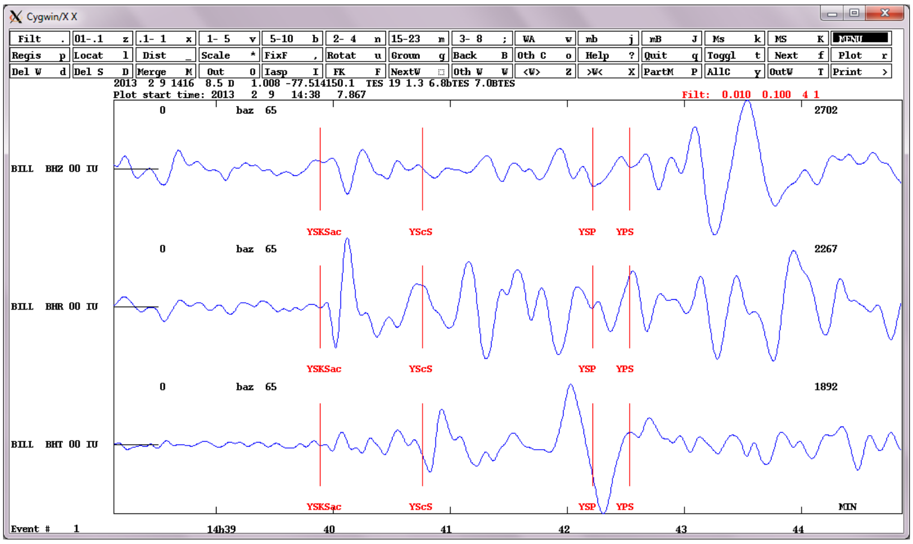

Three-component traces for station BILL at Δ = 98.6°, rotated and filtered 0.01-0.1 Hz: The two horizontal components have been rotated into radial and transverse components using a backazimuth of 65°. SKS has been back-converted from a P wave through the outer core, termed K, into an S wave through the mantle and is, therefore, polarised in the vertical plane of propagation. Accordingly, it has its largest amplitude in the radial component R (middle trace) and not on the transverse component T. It is also visible on the vertical component. This is not the rule for teleseismic S and illustrates that rotating seismograms can be useful in identifying seismic phases (see Figs. 11.12, 11.37 and 11.56 ?? in the Manual Chapter 11 of Bormann, 2009). Having an array of stations, the different apparent velocities of seismic phases can also be used for identification (see, e.g., Chapter 9, and for the identification of core phases Fig. 11.34 ?? in the Manual edition by Bormann (2009).

```
#    1  9 Feb 2013 14:16  8  D   1.008 -77.514150.1    1.3 6.8bTES   19  ? 1

  date hrmn   sec      lat      long depth   no m    rms  damp erln erlt erdp
13 2 9 1416  8.59  059.46N  77 28.5W 149.5   28 3   1.16 0.000 21.6 17.2  5.7
 stn  dist   azm  ain w phas    calcphs hrmn tsec  t-obs  t-cal    res   wt di
 LCO   3398 168.3 40.0 0 P       P       1422  9.6 360.99 359.70   1.29 1.00 10
 RCBR  4682  99.8 36.3 0 P       P       1423 45.0 456.39 457.12  -0.72 1.00  7
 PFO   5437 315.8 33.9 0 P       P       1424 39.4 510.86 510.52   0.35 1.00  7
 EFI   6121 165.4 31.7 0 P       P       1425 25.1 556.49 555.86   0.63 1.00  7
 EFI   6121 165.4      0 IVmB_BB         1425 28.3  559.7
 EFI   6121 165.4      0 IAmb            1426  9.7  601.1
 CMLA  6687  46.1 29.9 0 P       P       1425 59.1 590.53 591.50  -0.97 1.00  2
 CMLA  6687  46.1      0 IVmB_BB         1426  3.6  595.0
 CMLA  6687  46.1      0 IAmb            1426  4.2  595.6
 MACI  7140  59.0 28.5 0 P       P       1426 27.2 618.59 618.76  -0.17 1.00  2
 MACI  7140  59.0151.0 0 pP      pP      1427  3.7 655.14 654.18   0.96 1.00  5
 PAB   8504  49.6 24.3 0 P       P       1427 40.6 691.97 693.14  -1.17 1.00  1
 PAB   8504  49.6155.3 0 pP      pP      1428 18.2 729.56 729.75  -0.19 1.00  5
 PAB   8504  49.6 26.2 0 S       S       1437 15.41266.861266.68   0.18 1.00  8
 KDAK  9045 328.4 22.7 0 P       P       1428  6.6 717.97 719.55  -1.57 1.00  3
 BFO   9626  41.8 20.8 0 P       P       1428 32.9 744.36 746.02  -1.65 1.00  1
 BFO   9626  41.8      0 IVmB_BB         1428 37.2  748.6
 BFO   9626  41.8      0 IAmb            1428 37.9  749.4
 BFO   9626  41.8158.8 0 pP      pP      1429 11.1 782.48 783.45  -0.96 1.00  4
 KBS   9899  11.1 20.0 0 P       P       1428 45.8 757.23 757.65  -0.42 1.00  1
 KBS   9899  11.1      0 IAmb            1428 49.9  761.4
 KBS   9899  11.1      0 IVmB_BB         1428 51.9  763.3
 KBS   9899  11.1 35.6 0 PP      PP      1432 20.5 971.87 968.68   3.20 1.00  2
 KEV  10472  19.7 19.5 0 P       P       1429  8.0 779.44 781.44  -2.00 1.00  0
 KEV  10472  19.7      0 IAmb            1429 11.9  783.3
 KEV  10472  19.7      0 IVmB_BB         1429 13.5  784.9
 KEV  10472  19.7 26.5 0 SP      SP      1441 25.81517.181514.82   2.36 1.00  6
 BILL 10982 340.0 18.9 0 P       Pdif    1429 29.2 800.57 801.82  -1.25 1.00  2
 BILL 10982 340.0      0 IVmB_BB         1429 32.3  803.7
 BILL 10982 340.0      0 IAmb            1429 35.1  806.5
 BILL 10982 340.0 11.7 0 SKSac   SKSac   1439 53.61425.021425.40  -0.37 1.00  4
 KURK 13871  18.2  8.0 0 P       PKPdf   1434 49.31120.701121.34  -0.64 1.00  0
 NWAO 16181 202.1 13.2 0 P       PKPbc   1435 28.61159.981160.26  -0.28 1.00  3
 ENH  16499 348.5  6.8 0 P       PKPdf   1435 33.21164.591164.16   0.44 1.00  1
 KMI  17148 359.6  5.9 0 P       PKPdf   1435 42.81174.191173.26   0.94 1.00  1
 PALK 17448  69.0  5.4 0 P       PKPdf   1435 45.81177.261176.64   0.62 1.00  1
 CHTO 17812  10.0  4.8 0 PKPdf   PKPdf   1435 49.61181.041180.59   0.45 1.00  1
 CHTO 17812  10.0175.2 0 pPKPdf  pPKPdf  1436 28.51219.871220.40  -0.53 1.00  5
 CHTO 17812  10.0177.3 0 sPKPdf  sPKPdf  1436 45.41236.841235.95   0.89 1.00 10
 KAPI 18072 256.6  4.2 0 P       PKPdf   1435 52.21183.621183.05   0.57 1.00  2

2013  2 9 1416  8.6 D   0.991 -77.475149.5  TES 19 1.2 6.8bTES 7.0BTES
```

Output from the location program: Adding three pP phases and one pPKPdf and sPKPdf each, the hypocenter depth changes (shown in the third and last line) from 132 to 149 km. While this is now more different from the solution given by the USGS, we take this as the best solution determined from our data set, which may be even better than the USGS solution, because the latter commonly uses only P-wave first arrivals for their hypocenter location. Yet, the reading, proper identification and time picking of later arriving phases is crucial for significantly reducing the errors in hypocenter depth estimates (see Figure below).

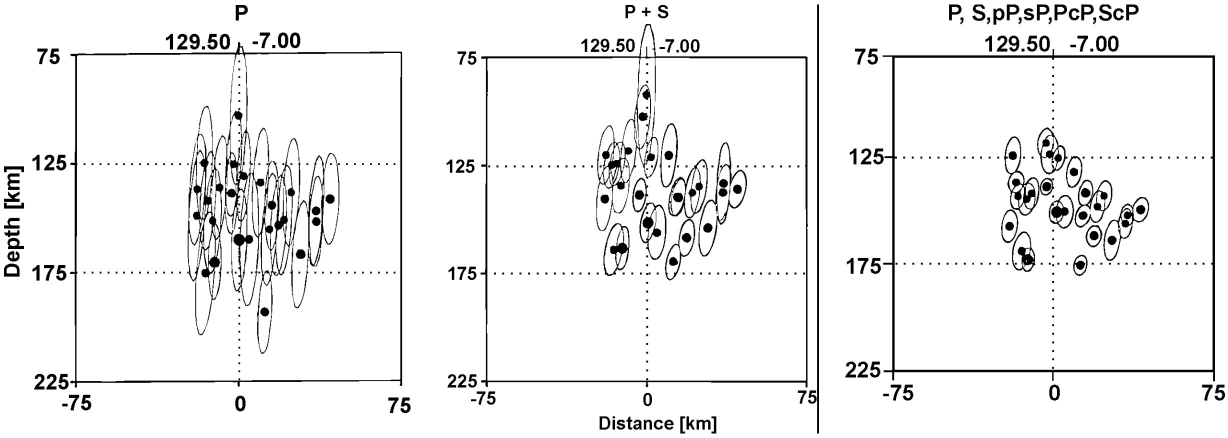

Left: hypocenter locations using only P phases; **middle:** by adding S phases; **right:** by adding also depth phases and core reflections. (Copy of Figure 7 from IS 11.1, modified from Schöffel and Das, J. Geophys. Res., Vol. 104, No. B6, page 13, Figure 2; © 1999, by permission of American Geophysical Union).

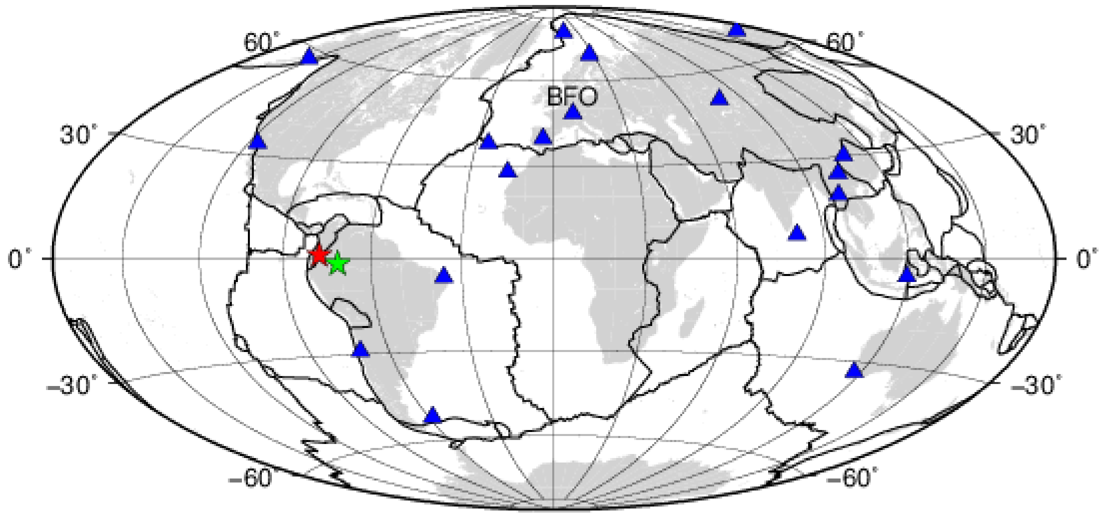

Map showing the epicenter of the Colombia earthquake (red star) determined by using a network of globally distributed stations (blue triangles). For comparison we plotted the epicenter from the single station (BFO, see label) 3-component location as a green star. For details of the BFO location see the next section.

6 Single station 3-component source location

So far we have demonstrated how data from a global network can be processed in SEISAN. This is nowadays the common procedure as the data from a large number of stations are now freely accessible via Internet. However, it is also possible with SEISAN to estimate the event location by analyzing only the three-component records of a single station. The epicentral distance of the station can be determined best from the time difference S-P, but also using time differences of P to other later phases such as PP, SP or even SS (see Fig. 11.23 of Chapter 11 in Bormann2009, and EX 11.2). SKS-P is not suitable, because this time difference does not change much with distance. The backazimuth can be determined from the amplitude ratios of the three components (see Figure 1 and text in IS 11.1 and EX 11.2). For the backazimuth calculation the method of Roberts et al. (1989) is implemented in SEISAN.

We start with the determination of the back-azimuth from the P-wave first-motion amplitudes, as we need the backazimuth to rotate the seismograms into the ZRT system, which we will use to identify the phases.

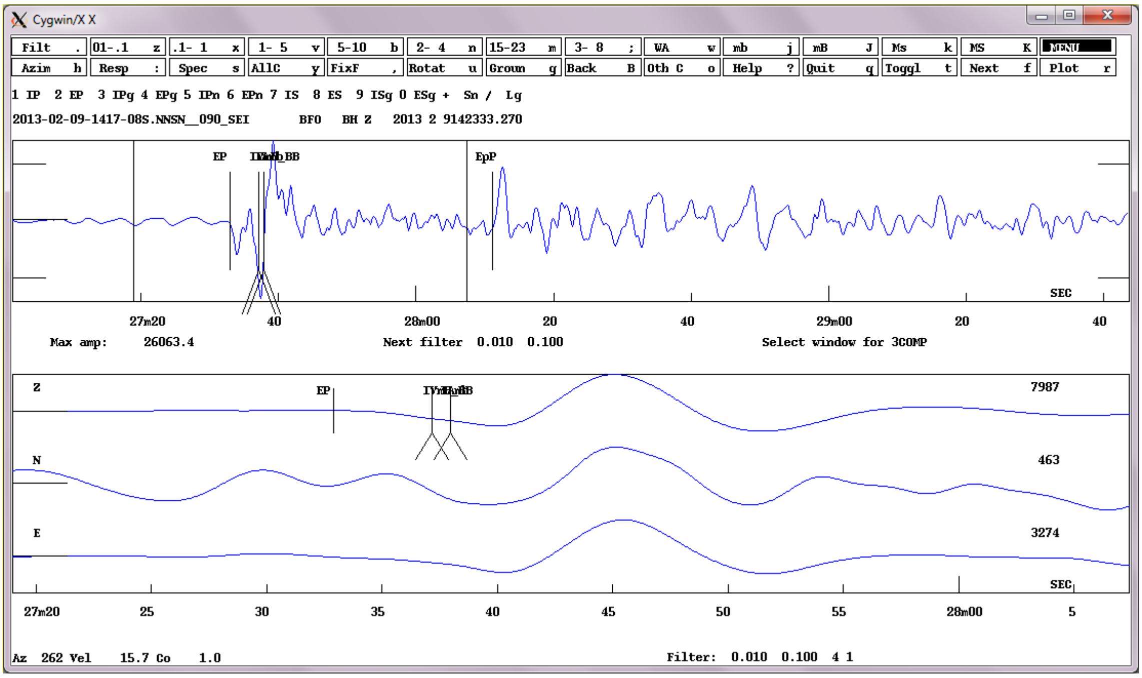

Three-component analysis of station BFO at Δ= 86.4°, filtered 0.01-0.1 Hz: From, the above trace plot we see a positive correlation between the vertical and the two horizontal components. By definition this means that first motion direction of P in the horizontal components shows toward the source, which is in the south-west. However, since the N-S amplitude is much smaller than the E-W amplitude (compare the numbers on the outermost right side of the traces), we can further conclude that the ray is coming more from the west than from the south thus matching for station BFO a backazimuth of 262°.

In the next step we estimate the epicentral distance via the time difference between P and identified later arriving phases.

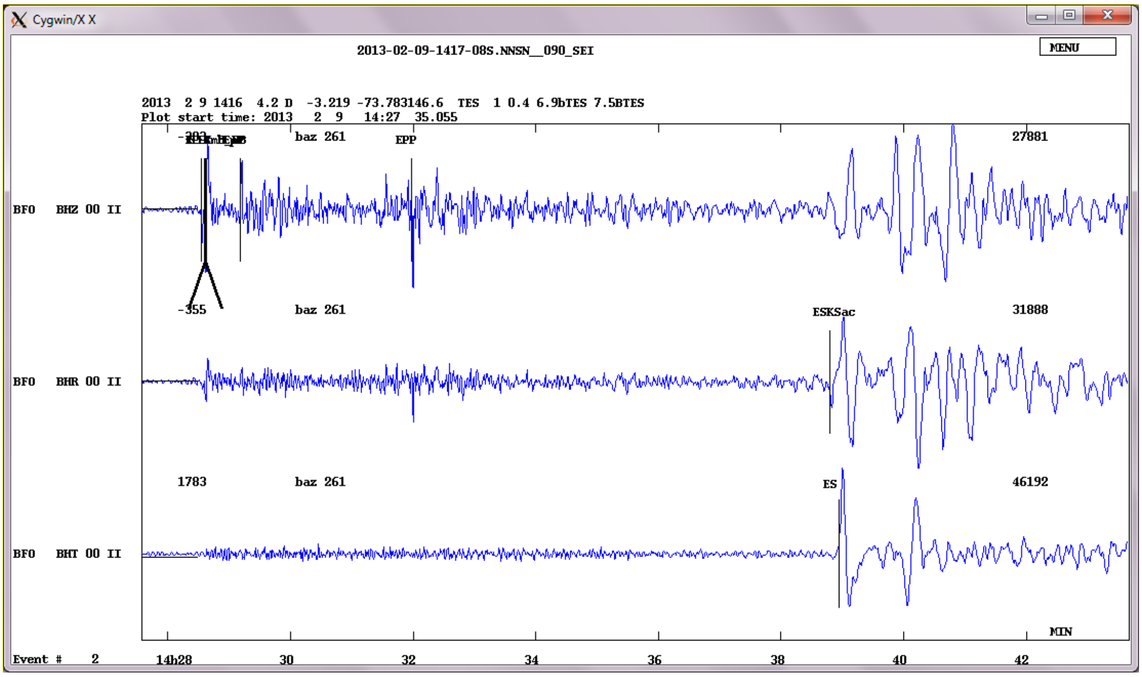

Three-component analysis of station BFO at Δ= *86.4°, unfiltered*: From the time difference between P with PP and S (here identified as SKS on the middle trace and as the slightly later arriving S on the bottom trace) we estimate the epicentral distance, assuming a source depth of 150 km according to the pP-P time (see Table below). This depth estimate agrees reasonably well with interpreting the strong onsets that follow SKS. S arrives about 13 s after SKS and the depth phase sS 74 s after S, corresponding at Δ= *86.4°* to a computed source depth of 170 km according to the IASP91 tables. This gives some feeling for the possible influence of errors in the assumed velocity model, phase interpretation and/or onset-time piking on the estimation of source depth.

We can either read the distance for which we get the best match between our observations and the travel time curves of the global IASP91 velocity model, or equivalently estimate it with a grid search by computing travel times for a range of distances as done here. In our example we then get Δ = 86.5° (see Table below). This differs only 0.15° from our first multi-station P-wave location (86.35°) and even less from our improved multi-station and multi-phase location (86.56°) (see above location program outputs). Together with the backazimuth we can now locate the event on a suitable stereographic map with station BFO in the center (as in Figure 12 of EX 11.2 for an Ecuador earthquake and station CLL).

Phase difference	**Time difference δt(s)**	**δt(s) for Δ = 86°**	**δt(s) for Δ = 87°**
PP-P	205.7	202	205
S-P	623.3	622	626

```
#    2  9 Feb 2013 14:16  1  D                                     ? 1

  date hrmn   sec      lat      long depth   no m    rms  damp erln erlt erdp
13 2 9 1416  4.23  312.63S  73 47.5W 146.6    5 2   0.37 0.000552.7488.0  0.0
 stn   dist   azm  ain w phas    calcphs hrmn tsec  t-obs  t-cal    res   wt di
 BFO   9700  41.4 14.4 0 SKSac   SKSac   1438 47.31363.051362.11   0.94 0.98*12
 BFO   9700  41.4 35.9 0 PP      PP      1431 58.6 954.40 954.80  -0.39 1.00*22
 BFO   9700  41.4      0                 1428 35.3  751.1
 BFO   9700  41.4159.1 0 pP      pP      1429 11.1 786.84 786.42   0.42 1.00*22
 BFO   9700  41.4      0 IAmb            1428 37.9  753.7
 BFO   9700  41.4      0 IVmB_BB         1428 37.2  753.0
 BFO   9700  41.4 20.4 0 P       P       1428 32.9 748.67 749.64  -0.97 0.97*11
 BFO   9700  41.4        AZ                         262.0  262.0   0.00 0.20 33

  2013  2 9 1416  4.2 D  -3.210 -73.792146.6  TES  1 0.4
```

Output from the location program: We can obtain a single-station three-component location, which is within 500 km from the one obtained by the standard location program with several stations. While our distance estimate is very good, we would have to get a 5° larger back-azimuth reading to get a location very close to the multi-station location. This shows the approximate range of uncertainty of single station locations in the far teleseismic range. Wrong phase interpretation may increase single station location errors. E.g., when interpreting in this case the earlier arriving SKS as S, the distance estimate from S-P would be 0.2° shorter in the case of BFO but this underestimation would increase for any station further away within the distance range where SKS arrives before S (see differential travel-time curve in Figure 4 of EX 11.2). For shallow earthquakes at Δ = 100° the error $\delta\Delta$ would reach already 0.9°. However, with proper S-P times, or when several other phases have also been correctly identified, the distance can generally be estimated, up to 160°, within 1-2° and the azimuth with P-wave first motion amplitudes, when measured with good signal-to-noise ratio on well calibrated 3-component seismometer components, within about 5-10°. This allows rather fast and reasonably good first location estimates even with single station data only (see Fig. 11.23 in Chapter 11 of NMSOP-1 in Bormann, 2009, and examples in EX 11.2).

Finally, we determine the teleseismic magnitudes for this earthquake. Since this is a deep earthquake, only the two teleseismic standard body-wave magnitudes mb and mB_BB should be calculated. Note, however, that the IASPEI WG on magnitudes encourages stations to measure according to the standard procedures also IAMs_20 and IVMs_BB with their periods if surface-waves are still clearly visible in records of deeper earthquakes as this is the case also for our example (see, e.g., in section 5, the record trace for station KADAK in the plot: *Vertical-component traces for which phases are picked, filtered 0.02-5 Hz*). Such data are of great interest for investigating the depth and period dependence of surface waves and to derive improved calibration functions $\sigma(\Delta,h,T)$. Note that for 20 s surface-waves and thus Ms_20 calculation such depth corrections have already been published by Herak et al. (2001):

$\Delta Ms(h) = 0$ for $h < 20$ km
$\Delta Ms(h) = 0.314\log(h) - 0.409$ for 20 km $\le h <$ 60 km
$\Delta Ms(h) = 1.351\log(h) - 2.253$ for 60 km $\le h <$ 100 km
$\Delta Ms(h) = 0.400\log(h) - 0.350$ for 100 km $\le h <$ 600 km.

For station KDAK, e.g., one would measure IAMs_20 = 10078 nm at T = 19 s and thus get a depth corrected Ms_20 = 6.2 + 0.5 = 6.7 which compares rather well with our body-wave magnitudes mb = 6.8 and mB_BB = 7.0 determined in the following.

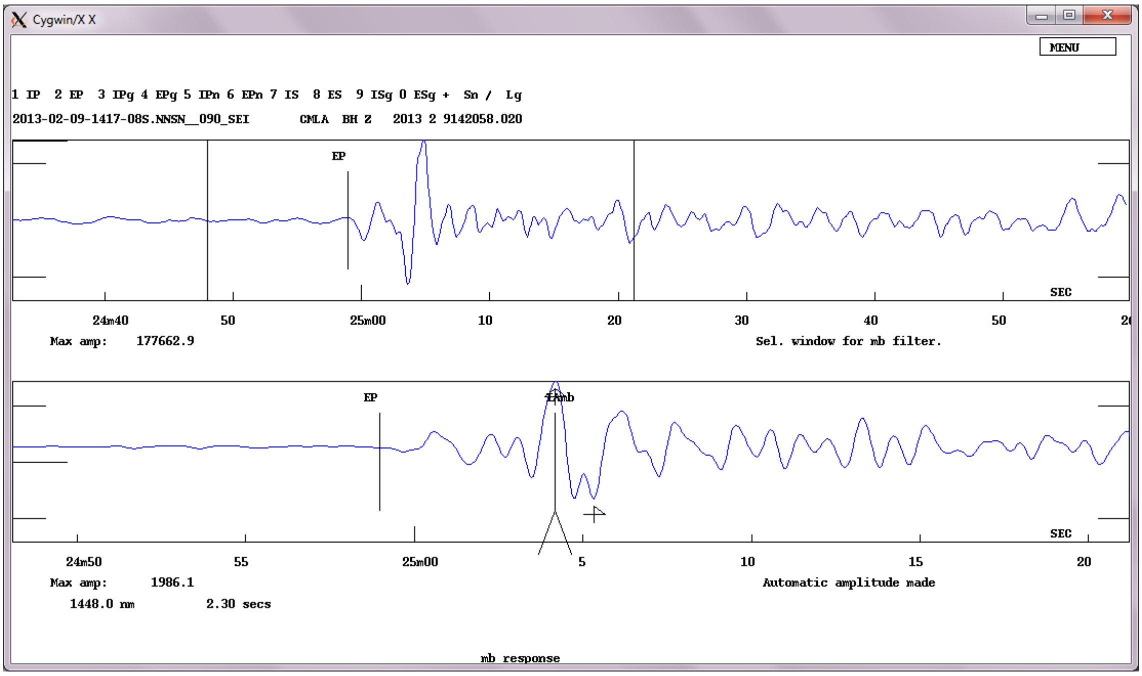

Amplitude reading for mb magnitude at station CMLA at Δ= 59.9°: As in the case of the regional event, the upper broadband trace is converted into a WWSSN short period trace (lower trace) on which the amplitude IAmb is read, here as 1148 nm with a period of 2.3 s.

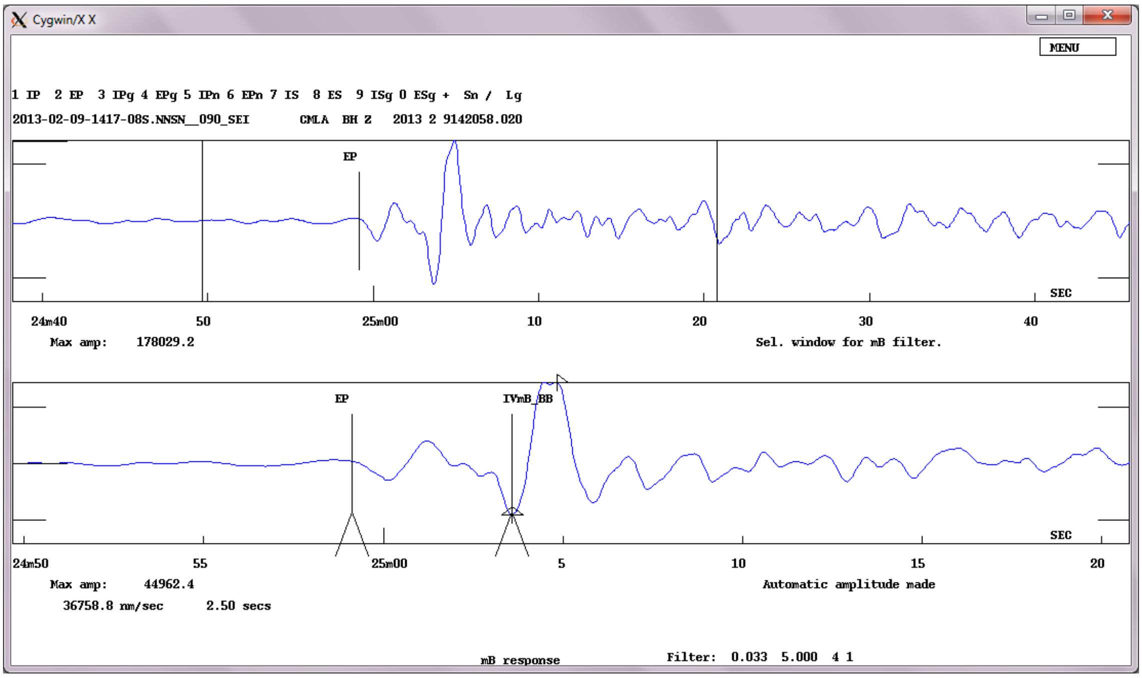

Amplitude reading for mB_BB magnitude at station CMLA at Δ=59.9°: As in the case of the regional event the amplitude IVmB_BB is read on the bottom trace that has been deconvolved into a broadband velocity trace (top trace shows uncorrected data, which are in the case of a broadband seismometer also proportional to velocity): here 36758 nm/s with a period of 2.5 s.

Computing the average magnitudes from all station amplitude observations we get the values below. In this case mB_BB is equal to Mw, and mb is only slightly smaller. Since the period at which mb is read is almost the same as for mB_BB the difference is mainly due to the larger bandwidth of the broadband record.

Magnitude scale	Value
Mw (USGS)	7.0
mb	6.8
mB_BB	7.0

The following station amplitude readings were used in the event magnitude computation:

```
EFI  BZ    dist:    6121.0   amp:       13012.5 T:   2.7   mB =   6.9
EFI  BZ    dist:    6121.0   amp:         788.3 T:   1.1   mb =   6.5
CMLA BZ    dist:    6687.0   amp:       36756.6 T:   2.5   mb =   7.9
CMLA BZ    dist:    6687.0   amp:       36758.8 T:   2.5   mB =   7.5
CMLA BZ    dist:    6687.0   amp:       16414.7 T:   2.3   mb =   7.6
KEV  BZ    dist:   10472.0   amp:          83.5 T:   0.8   mb =   6.0
KEV  BZ    dist:   10472.0   amp:        2421.2 T:   5.5   mB =   6.6
KBS  BZ    dist:    9899.0   amp:         500.9 T:   0.9   mb =   6.5
KBS  BZ    dist:    9899.0   amp:       11474.4 T:   7.2   mB =   7.1
BFO  BZ    dist:    9626.0   amp:       34897.1 T:   3.7   mB =   7.4
BFO  BZ    dist:    9626.0   amp:        1747.1 T:   1.1   mb =   6.9
BILL BZ    dist:   10982.0   amp:        1555.7 T:   6.0   mB =   6.7
BILL BZ    dist:   10982.0   amp:         106.9 T:   1.2   mb =   6.3
```

7 Concluding remarks

The examples given here are meant to illustrate how the data processing is done using the SEISAN software and to illustrate some basic concepts of earthquake data processing. The examples should help newcomers to earthquake data processing to get started. It will be necessary to first learn SEISAN, but then the data used can be downloaded and the steps shown here followed. When analyzing seismograms, the number of phases that can be read depends on the earthquake size and thus the SNR of the recording, the epicentral distance, the source depth as well as on the bandwidth and period range of the seismic records (see Figs. 2.57-2.61 in Chapter 2). From a scientific perspective we wish to have as many good phases read as possible. However, there is often a limitation of how much can be done due to time constraints. We encourage the reader to read more than the first arriving P, and at least to identify clear additional later phases. A good exercise is to download data from the IRIS Wilber, take the data into SEISAN and start processing.

Acknowledgments

Our thanks go to Jens Havskov, Won-Young Kim and James Dewey. Their review comments helped to improve this manuscript.

References

Alsaker, A., Kvamme, L. B., Hansen, R. A., Dahle, A., and Bungum, H. (1991). The M_L scale in Norway. *Bull. Seism. Soc. Am.*, **81**, 2, 379-389.

Archangelskaya, V. M. (1959). The dispersion of surface waves in the earth's crust. *Izv. Akad. Nauk SSSR*, *Seriya Geofiz*., **9** (in Russian).

Bormann, P. (ed,) (2009). *New Manual of Seismological Observatory Practice*. Vol. 1 and Vol. 2, IASPEI, GFZ German Research Centre for Geosciences, Potsdam; electronic edition, accessible via http://nmsop.gfz-potsdam.de; DOI: 10.2312/GFZ.NMSOP_r1

Bormann, P. (2011). Earthquake magnitude. In: Harsh Gupta (ed.). *Encyclopedia of Solid Earth Geophysics,* Springer, 207-218; doi: 10.1007/978-90-481-8702-7.

Bormann, P., and D. Di Giacomo (2011). The moment magnitude M_w and the energy magnitude M_e: common roots and differences. *J. Seismology*, **15**, 411-427; doi: 10.1007/s10950-010-9219-2.

Braunmiller, J., Deichmann, N., Giardini, D., Wiemer, St., and the SED Magnitude Working Group (2005). Homogeneous moment-magnitude calibration in Switzerland. *Bull. Seism. Soc. Am*., **95**, 1, 58-74.

Choy, G. L. (2012). IS 3.5: Stress conditions inferable from modern magnitudes: development of a model of fault maturity. In: Bormann, P. (Ed.) (2012). *New Manual of Seismological Observatory Practice (NMSOP-2)*, *IASPEI,* GFZ German Research Centre for Geosciences, Potsdam, 10 pp.; doi: 10.2312/GFZ.NMSOP-2_IS_35.

Eshelby, J. (1957). The determination of the elastic field of an ellipsoidal inclusion and related problems. *Proc. R. Soc. London A*, 241, 376–396.

Gorbunova, I. V., and Kondorskaya, N. V. (1977). Magnitudes in the seismological practice of the USSR. *Izv. Akad. Nauk SSSR, ser Fizika Zemli*, No. 2, Moscow (in Russian).

Havskov, J. and Ottemöller, L. (2010). Routine Data Processing in Earthquake Seismology, With Sample Data, Exercises and Software. Springer, 380p.Herak, M., Panza, G., and Costa, G. (2001). Theoretical and observed depth corrections for Ms. *Pure Appl. Geophys*., **158**, 1517-1530.

Herak, M., Panza, G., and Costa, G. (2001). Theoretical and observed depth corrections for Ms. *Pure Appl. Geophys*., **158**, 1517-1530.

Hutton, L. K. and Boore, D. (1987). The Ml scale in Southern California. *Bull. Seismol. Soc. Am.*, 77:2074–2094.

IASPEI (2013). Summary of Magnitude Working Group recommendations on standard procedures for determining earthquake magnitudes from digital data.

http://www.iaspei.org/commissions/CSOI/Summary_WG_recommendations_20130327.pdf

Lienert, B. R. E., Berg, E., and Frazer, L. N. (1986). Hypocenter: An earthquake location method using centered, scaled, and adaptively damped least squares. *Bull. Seismol. Soc. Am.*, 76:771–783.

Lienert, B. R. E. and Havskov, J. (1995). A computer program for locating earthquakes both locally and globally. *Seism. Res. Lett.*, 66:26–36.

Richter, C. F. (1935). Elementary seismology, W. H. Freeman and Co., San Francisco, 578p.

Roberts, R. G., Christoffersson, A., and Cassidy, F. (1989). Real time events detection, phase identificationand source location estimation using single station component seismic data and a small PC. Geophys. J. Int., 97:471–480.

Schöffel, H.-J. and Das, S. (1999). Fine details of the Wadati-Benioff zone under Indonesia and its geodynamic implications. *J. Geophys. Res*., **104**, 13101-13114.

Uhrhammer, R. A., and Collins, E. R. (1990). Synthesis of Wood-Anderson seismograms from broadband digital records. *Bull. Seism. Soc. Am*., **80**, 702-716.

Utsu, T. (2002). Relationships between magnitude scales. In: *International Handbook of Earthquake and Engineering Seismology*, *Part A*, edited by W.H.K. Lee, H. Kanamori, P.C. Jennings, and C. Kisslinger, Academic Press, Amsterdam, 733–746.